Journal of Power Sources 634 (2025) 236496

Contents lists available at ScienceDirect

Journal of Power Sources

journal homepage: www.elsevier.com/locate/jpowsour

# Cell design and chemistry of commercial sodium-ion battery cells

Vittorio Marangon [a,b,1], Katharina Bischof [c,1], Aislim Aracil Regalado [c], Miriam Keppeler [c], Mariam Pogosova [a,b], Mintao Wan [a,b], Jaehoon Choi [a,b], Simon Fleischmann [a,b], Thomas Diemant [a,b], Margret Wohlfahrt-Mehrens [a,c], Markus Hölzle [c,d], Thomas Waldmann [a,c,d,**], Dominic Bresser [a,b,d,*]

[a] Helmholtz Institute Ulm (HIU), Helmholtzstrasse 11, 89081, Ulm, Germany
[b] Karlsruhe Institute of Technology (KIT), P.O. Box 3640, 76021, Karlsruhe, Germany
[c] Zentrum für Sonnenenergie- und Wasserstoff-Forschung Baden-Württemberg (ZSW), Helmholtzstrasse 8, 89081, Ulm, Germany
[d] Ulm University (UUlm), 89069, Ulm, Germany

## HIGHLIGHTS

- In-depth investigation of commercial 18650 sodium-ion battery cells.
- Assessment of the cell design parameters and electrode arrangement.
- Physicochemical characterization of the hard carbon anode and layered oxide cathode.
- Testing of the anode and cathode in half-cells.
- Electrochemical evaluation of the 18650 full-cells under challenging conditions.

## GRAPHICAL ABSTRACT

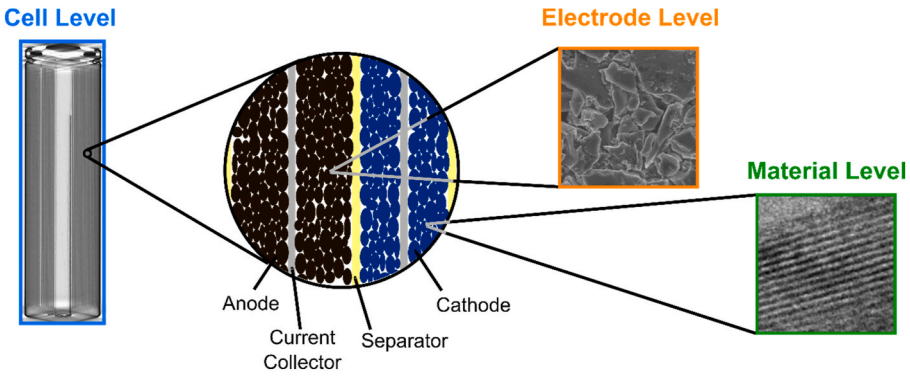


## ARTICLE INFO

*Keywords:*
Sodium-ion battery
Commercial cell
18650 cylindrical cell
Layered oxide cathode
Hard carbon anode
Organic carbonate electrolyte

## ABSTRACT

Commercially available 18650-type cylindrical sodium-ion battery (SIB) cells with a nominal capacity of 1.5 Ah are comprehensively investigated, yielding in-depth insights into the cell design, the chemical composition of the electrodes and the electrolyte composition. In addition, the performance of single electrodes as well as the complete cell as such – under both standard and harsher conditions – are investigated. The results reveal superior charge storage kinetics at the $Na_xNi_yFe_zMn_{1-y-z}O_2$-based cathode and rather sluggish kinetics at the hard carbon negative electrode, while the analysis of the already formed interphase indicates the presence of functional additives in the organic carbonate-based electrolyte. As such, this study reports a multi-disciplinary approach to assess the most relevant characteristics of commercial(-type) cells from the macro-scale to the micro-scale.

* Corresponding author. Helmholtz Institute Ulm (HIU), Helmholtzstrasse 11, 89081, Ulm, Germany.
** Corresponding author. Zentrum für Sonnenenergie- und Wasserstoff-Forschung Baden-Württemberg (ZSW), Helmholtzstrasse 8, 89081, Ulm, Germany.
*E-mail addresses:* thomas.waldmann@zsw-bw.de (T. Waldmann), dominic.bresser@kit.edu (D. Bresser).
[1] These authors contributed equally.

https://doi.org/10.1016/j.jpowsour.2025.236496
Received 19 December 2024; Received in revised form 30 January 2025; Accepted 7 February 2025
Available online 16 February 2025

## 1. Introduction

In recent years, sodium-ion batteries (SIBs) attracted relevant interest due to the growing efforts to find sustainable energy storage systems as alternative to presently used lithium-ion batteries (LIBs) in electric vehicles, portable electronics and stationary power grids [1,2]. Despite the high specific energy close to 300 Wh $kg^{-1}$ achieved by LIBs [3,4], they still rely on critical raw materials such as lithium, cobalt and copper, which poses concerns due to their limited abundance, high production costs, and, in particular for cobalt, toxicity [5,6]. Hence, the replacement of lithium with sodium in such rechargeable batteries represents a rational choice in view of the reduction of cost triggered by the much higher abundance of sodium in the Earth crust compared to lithium [7,8]. Sodium-containing electrodes exploit the same rocking chair ion exchange mechanism, but rely on eco-friendlier and more cost-effective electrode compositions [4,9,10]. In addition, at the anode side a rather cheap aluminum current collector can be used instead of copper as in LIBs, since sodium does not form any Na-Al alloy at low potentials. Graphite, used in LIBs for the anode, can be substituted with hard carbon materials, which can also be efficiently synthetized from bio-waste resources, such as peanut shells [11,12], hazelnut shells [13], cellulose [14,15], bamboo [16], coffee powder [17], and many others [18]. At the cathode side, various structures and chemistries have been established in advanced SIBs. In the first place, layered oxide materials with either the P2- or O3-type structure and the general formula $Na_xMO_2$ (where M is a transition metal or a combination of them) represent one of the most promising solutions due to their very good performance and the analogy to Li-based materials sharing the same – or at least very similar – structure and charge storage mechanism (e.g., $LiCoO_2$ or the more advanced $LiNi_{1-y-z}Mn_yCo_zO_2$, i.e., NMC) [19]. Polyanionic compounds with various crystalline structures containing the $PO_4$ group are also drawing increasing interest due to their rather high operating voltage, delivered capacity and structural stability. Examples are vanadium-based NASICON-type $Na_3V_2(PO_4)_3$, the $NaVPO_4X$ (X = O, F) family [20], or the olivine-structured $NaMnPO_4$, $NaFePO_4$ and $NaFe_{1-x}Mn_xPO_4$ [21]. In addition, Prussian blue analogues with the general formula $Na_xM[M'(CN)_6]_y{\cdot}zH_2O$ demonstrated promising performance [22]. In this scenario, the extensive research on SIBs led to the development of commercial-type prototypes at the lab scale, including 18650-type cylindrical cells combining a hard carbon anode and either polyanionic $Na_3V_2(PO_4)F_3$ [23,24] or the Prussian Blue analog $Na_2Fe_2(CN)_6$ [25] as cathode active material, and 26650-type cylindrical cells using a Cu-based layered sodium transition metal oxide cathode [26]. These extensive efforts allowed for the recent commercialization of the first cylindrical SIB cells relying on hard carbon anodes and exploiting either $Na_3V_2(PO_4)_2F_3$ [27] or a layered sodium transition metal oxide [28–31] as the cathode. In a recent report, we provided a first systematic investigation of commercially available 18650 and 26700 SIB cells with nominal capacities of 1.5 Ah and 3.5 Ah, respectively, and compared the data with LIBs owning advanced configurations from pouch-type to cylindrical [32]. This study demonstrated that commercial SIB cells today already can well compete with LiFePO$_4$-based LIBs in terms of specific energy, cell impedance, and thermal properties [32], underlining the intrinsic potential of this emerging technology. On the other hand, further improvements are required to make such battery cells a serious competitor of LIBs in a wide array of applications. Therefore, in the present work, we provide a systematic study on the 1.5 Ah 18650 SIB commercial cells to assess all details, from the macro-scale to the micro-scale. The 18650 SIB cells are firstly investigated in terms of design and physical arrangement of the electrodes in the jelly roll, followed by a thorough examination of the electrode composition and their electrochemistry. Finally, the electrochemical performance of the 18650 SIB cells is evaluated under challenging conditions to get a good understanding of their potential performance. The resulting thorough understanding of these recently commercialized SIB cells is of key importance for having a reference for further research, including not least the development of new materials. In fact, only when knowing in detail the current state of the art of this rather novel technology (with regard to its commercialization), meaningful research can be conducted that may help to get beyond the state of the art. This is even more important in this particular case, as there are a lot of numbers concerning specific energy etc. that have been announced by companies, but could not be independently confirmed, yet. To the best of our knowledge, our study is at least one of the first to do so, and certainly the one investigating commercial cells with the highest specific energy independently reported so far.

## 2. Experimental

### 2.1. Basic characterization of the cells

A commercial 18650-type SIB cell with a nominal capacity of 1.5 Ah was investigated. In addition to the cells from our previous study (batch 1) [32], a second batch of 200 cells was purchased (batch 2). Upon arrival, these cells were first tested regarding their mass, voltage, and internal resistance prior to further use. An average mass of (36.72 ± 0.17) g was determined. The voltage and the corresponding internal resistance at 1 kHz, measured with a Hioki BATTERY HiTESTER 3554, were 2.568 ± 0.002 V and 19.6 ± 0.3 mΩ, respectively. The standard deviations of all measured values are in the range of 1–2% and therefore comparably low to commercial 18650 LIB cells [33,34], making the herein studied SIB cells suitable for further investigations.

In order to identify the quality of the SIB cells and to uncover manufacturing-related defects in a non-destructive manner, X-ray computed tomography (CT) scans were performed using a GE Phoenix v|tome|x m system with a microfocus X-ray tube (voltage: 122 kV, current: 290 μA). The samples were rotated by 360° during the measurement, with a projection acquired at a defined degree-fraction, resulting in 1000 individual images. Subsequently, the CT data were processed using the Datos reconstruction software to obtain 3D representations of the sample. For the detailed analysis, 2D regions of interest (ROIs) were extracted and processed using the Volume Graphics myVGL 2.2 software. A grayscale analysis was carried out, where materials with high density and atomic number (high radiation absorption), such as the cell casing and the current collector tabs, exhibit lower grayscale values.

To gain information on the cell design and the cell chemistry, pristine cells were subjected to an *ex situ* analysis, i.e., opened and disassembled in the fully discharged state (1.5 V) in an Ar-filled glovebox (MBraun, $H_2O$ and $O_2$ levels below 0.1 ppm). The electrode dimensions such as the length and width of the current collector foils as well as the coated areas were measured under Ar atmosphere. A batch of wet electrodes was directly sealed in vials to perform headspace gas chromatography-mass spectrometry (GC-MS) on the electrolyte used in the SIB cell, using a Clarus 680 gas chromatograph coupled with a Clarus 600T quadrupole mass spectrometer from PerkinElmer.

Differential scanning calorimetry (DSC) was conducted on the separator of the SIB cell with a DSC 204 F1 instrument from Netzsch. The sample crucible and the reference crucible filled with $Al_2O_3$ were simultaneously heated twice from 30 °C to 220 °C at a rate of 5 °C $min^{-1}$, and the measured temperature difference between the sample and the reference was converted into a heat flow, which corresponds to endothermic or exothermic reactions of the sample.

### 2.2. Physicochemical characterization of the electrodes

After dimensional evaluation, the electrodes obtained from the 18650 SIB cells were washed three times with dimethyl carbonate (DMC, ≥99 %, anhydrous, Sigma-Aldrich) for 1 min each and subsequently dried under vacuum. The *ex situ* scanning electron microscopy (SEM) analyses of the electrodes were performed using a ZEISS Crossbeam XB340 instrument equipped with an energy dispersive X-ray (EDX) spectrometer (Ultim Extreme™, Oxford instruments). The cross-

sectional electrode samples were prepared using a Capella focused ion beam (FIB) with a gallium ion source, utilizing a course milling current of 65 nA, followed by a fine milling current of 7 nA. The cross-section images were captured following FIB milling by using the SmartSEM software for tilt correction to compensate for any image distortion arising from the 54° tilt from the optical axis. The same electron microscope was employed with an accelerating voltage of 5 kV to capture additional images of the electrode surface.

The electrode thicknesses, which are averages of ten measurements at different positions along the jelly roll, were determined with a micrometer gauge. Mercury intrusion porosimetry (MIP) measurements were performed on the electrodes using a PASCAL 140–440 Series porosimeter from Porotec. The surface tension and the contact angle of mercury were set to 0.48 N $m^{-1}$ and 140°, respectively, and the pressure was increased stepwise with a speed of 6–19 MPa $min^{-1}$, until a maximum pressure of 375 MPa was reached.

X-ray diffraction (XRD) patterns were recorded using a Bruker D8 Advance (Cu-K$\alpha_{1,2}$ radiation; SSD160-2detector; 2.5° soller slits; 9.5 mm fixed divergence slit) in the 2θ range from 10° to 120° for the cathode and between 10° and 90° for the anode, with a 2θ step size of 0.01°. The experimental conditions for the cathode were set to achieve XRD pattern intensities exceeding 12,000 counts. The XRD pattern recorded for the cathode active material was refined by the Rietveld method in the R-3m space group using the JANA 2020 software [35]. The initial LeBail refinement settings were as follows: background: manual in combination with the Chebyshev polynomial with 5 variables; vertical shift: *Sycos*; unit cell dimensions: *a* and *c*; profile: Pseudo-Voigt peak-shape function with GW, LY, LX. The structure refinement parameters were as follows: atomic position *z* of oxygen (coordinates for Na, Fe, Mn, and Ni positions were fixed); thermal displacement parameters: isotropic approximation for all ions; occupancy of Na (occupancies for Fe, Mn, and Ni were entered as 1/3 and fixed). A schematic representation of the crystal structure of the cathode active material was obtained using the Diamond 4.6.8. software.

Transmission electron microscopy (TEM) was conducted on the coating powders using a Talos F200i microscope (Thermo Fisher Scientific) operating at an accelerating voltage of 200 kV. Selected area electron diffraction (SAED) patterns were collected using a 10 μm selected area aperture. EDX mapping analysis was performed in scanning transmission electron microscopy (STEM) mode using Dual Bruker XFlash 6–100 DES detectors.

X-ray photoelectron spectroscopy (XPS) measurements were carried out both on electrodes and coating powder of the cathode with a Specs XPS system. To avoid surface contamination, the samples were transferred after preparation in inert gas atmosphere to the sample load lock of the XPS system. The measurements were acquired using monochromatized Al Kα radiation (300 W, 15 kV) and pass energies of 90 and 30 eV for survey and detail measurements, respectively. All binding energies were calibrated with the C 1s peak of adventitious carbon at 284.8 eV. The CasaXPS software was employed for the peak fit of the XPS results using Shirley-type backgrounds together with Gaussian-Lorentzian (GL30) peak shapes. Single-coated anodes and cathodes were obtained by removing one of the slurry coatings using deionized water under ambient atmosphere. The single-coated tapes were subsequently cut into 12 mm-diameter discs and dried under vacuum at 110 °C for 3 h before transferring them into an Ar-filled glovebox (MBraun, $H_2O$ and $O_2$ level below 0.1 ppm). Bare aluminum current collectors were obtained from the anode and cathode by removing the electrode coatings using deionized water. Prior to any further analysis, the Al current collectors were dried under vacuum to remove possible traces of water. The thicknesses of the current collectors were calculated based on the mass per unit area and the density of Al being 2.7 g $cm^{-3}$. SEM micrographs of the Al current collectors were acquired using a Zeiss LEO 1550 microscope operating at an accelerating voltage of 5 kV.

### 2.3. Electrochemical evaluation of the electrodes and cells

Single-side coated electrodes were used in Na half-cells in either coin-type (CR2032, S4R company) or Swagelok-type cells. The half-cells were assembled by stacking a 12 mm Na metal disc (Acros Organics) as negative electrode, a glass fiber GF/D Whatman® separator with diameter of either 10 or 16 mm for Swagelok and coin-type cells, respectively, and a 12 mm single-side coated electrode. The Swagelok cells were assembled in a three-electrode configuration by using a third Na metal electrode as quasi-reference. The electrolyte used in Na half-cells was prepared by mixing ethylene carbonate (EC, ≥99 %, acid <10 ppm, $H_2O$ < 10 ppm, Sigma-Aldrich) and propylene carbonate (PC, ≥99 %, acid <10 ppm, $H_2O$ < 10 ppm, Sigma-Aldrich) as solvents in a 1:1 wt ratio, sodium hexafluorophosphate ($NaPF_6$, battery grade, Fluorochem) as conducting salt with a concentration of 1 mol $L^{-1}$ (1M), and fluoroethylene carbonate (FEC, battery grade, Sigma-Aldrich) with a concentration of 2 wt% with respect to the solvents-salt mixture. Cyclic voltammetry (CV) was performed on three-electrode cells between 0.02 and 2.0 V vs. $Na^+$/Na for the anode and between 2.0 and 4.1 V vs. $Na^+$/Na for the cathode at a sweep rate of 0.1 mV $s^{-1}$. Electrochemical impedance spectroscopy (EIS) was carried out upon CV at the open circuit voltage (OCV) of the cell, as well as after the 1st and 5th cycle within the 500 kHz–100 mHz frequency range using a voltage amplitude of 10 mV. Two-electrode Na half-cells (coin-cells) were subjected to galvanostatic charge/discharge cycling at a specific current of 1 mA $g^{-1}_{coating}$ between 0.02 and 2.0 V for the anode and between 2.0 and 4.1 V for the cathode. All the Nyquist plots of the EIS data were analyzed through the non-linear least-squares (NLLS) fitting method with the aid of the Boukamp software [36,37]. Only fits with a $\chi^2$ value of the order of $10^{-4}$ or lower were accepted. CV and EIS measurements were recorded via a multi-channel VMP3 potentiostat-galvanostat (Biologic Science Instruments), while galvanostatic tests were conducted using a MACCOR Series 4000 battery test system. The operating temperature for all the electrochemical measurements was 20 °C.

The electrochemical performance of the 18650 cells was evaluated in asymmetrical rate capability tests in the voltage range between 1.5 V and 4.1 V. First, a discharge rate capability test, then a charge rate capability test was performed. The discharge rate capability tests were performed prior to the charge rate capability tests in order to exclude effects of possible Na deposition for the former. During the first 24 cycles (i.e., the discharge rate capability part of the tests) the C rate in the constant current– constant voltage charging steps was fixed to C/2 with a cut-off current of C/20 (1C = 1.5 A) in the constant voltage phase, and the cells were discharged three times at each C rate of C/10, C/5, C/3, C/2, 1C, 2C, 3C, and then again at C/10 in constant current mode. After the discharge rate capability test, the discharge C rate was fixed to C/2 in the following 29 cycles for the charge rate capability part of the tests. The cells were charged in constant current mode three times per tested C rate (C/10, C/5, C/3, C/2, 1C, 3/2C, 2C, and C/10). One cycle with a C/10 charge step was implemented before each increase in C rate. In between all charge and discharge steps, the cells were allowed to rest for 1 h. All electrochemical measurements performed on the 18650 cells were conducted with five cells at room temperature using a BaSyTec CTS battery test system.

## 3. Results and discussion

Fig. 1 reports the CT investigation of the pristine 18650 SIB cell and the dimensional evaluations of the electrode jelly rolls. Fig. 1a–e shows the results of the CT analysis, where materials with high density, i.e., the electrodes, current collector tabs, and the cell housing, exhibit high radiation absorption and are therefore displayed in darker grey in the scans. The frontal 2D cross-sections near the positive (Fig. 1a) and the negative (Fig. 1b) terminals of the cell reveal a cathode current collector tab which is connected to the positive terminal, while the anode current collector tabs are fixed to the negative terminal. Regarding the electrode

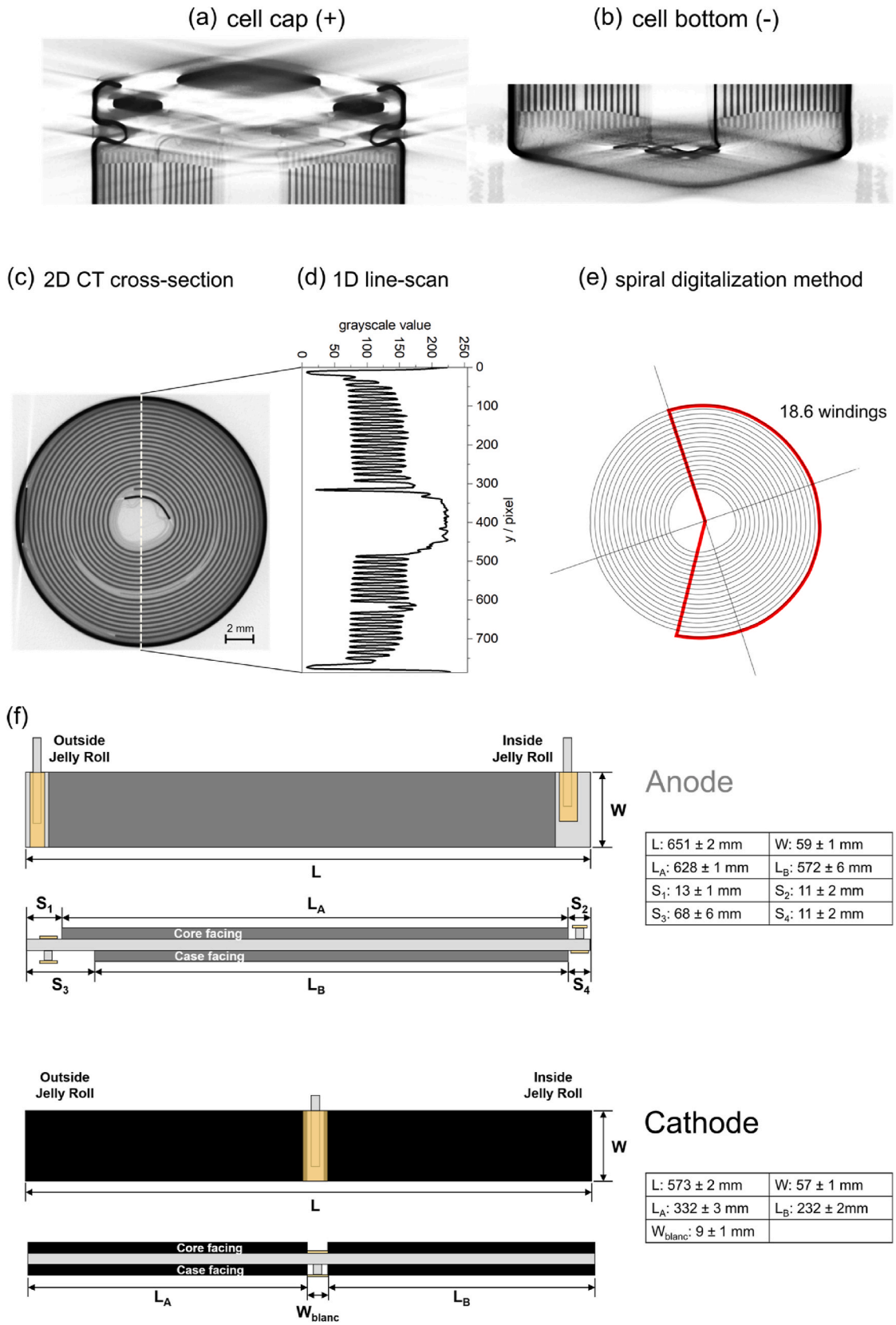


**Fig. 1.** **(a–e)** X-ray CT analysis of a pristine 18650 SIB cell: **(a, b)** frontal 2D cross-section CT near **(a)** the positive and **(b)** the negative terminal; **(c)** axial 2D cross-section CT at mid-height of the cylinder with **(d)** a grayscale value profile along the dashed line in the CT image and **(e)** the digitalization of the spiral. **(f)** Schematic representation of the cell design of the 18650 SIB cell. The values given for the dimensions of the electrodes correspond to the mean value of three cells from batch 2 (see the Experimental section for details).

alignment, it can be seen in Fig. 1a and b that the electrode layers are uniformly arranged in the outer and middle parts of the jelly roll. Only in the inner part near the core of the jelly roll, the electrode layers appear to be shifted towards the negative terminal. This effect most probably results from the winding process since the shift is similar on both sides of the jelly roll (compare Fig. 1a and b). However, this asymmetry is not as pronounced as recently reported for another type of an early commercial 18650 SIB cell, which was also affected by blended ends of the electrode layers [28].

Fig. 1c depicts an axial 2D cross-section of the CT data at mid-height of the cell cylinder, presenting the wound jelly roll without any deformations. The axial cross-section reveals two anode current collector tabs, which are located at the outer-most and the inner-most range of the jelly roll. In contrast, the cathode current collector tab is positioned in the middle part region of the jelly roll. All of these three arrestor tabs have no burrs and there are no other indications of manufacturing-related defects. A similar tab design was also reported for LIB cells [38–40], in fact.

Fig. 1d shows the line scan along the dashed line in the axial CT cross-section (Fig. 1c). The peaks of significantly low grayscale values in Fig. 1d (dark grey in Fig. 1c) can be assigned to the cell housing and the anode current collector tab near the core. The peak with the highest grayscale value in the periodic part of Fig. 1d (light grey in Fig. 1c) correlates with the location of the cathode current collector tab, while the curve profiles from pixel 600 to 650 with slightly higher grayscale values than in the neighboring regions is due to the bare aluminum current collector foils, likely arising from minor irregularities in the electrode winding, as also suggested by the corresponding CT region in Fig. 1c. The periodicity of the grayscale values along the cross-section allows for the determination of the approximate number of windings in the jelly roll by counting the peak maxima in the line profile [34]. A total of 38 peaks was identified, corresponding to approximately 19 windings for the 18650 SIB cell. In order to measure the exact number of windings, the spiral digitization method described in our previous work was used [41]. For this method, the windings of the jelly roll are digitized by superimposing them with a line that takes into account the exact start and end angle of the jelly roll. The resulting spiral-like line for the commercial SIB cell is depicted in Fig. 1e. The number of windings calculated by this method is 18.6, which is in the same order of magnitude as for cylindrical 18650 LIB cells [34,41–43], while 21700 LIB cells present a higher number of windings using the same electrodes [34,41]. After the non-destructive characterization of the 18650 SIB cells, pristine cells were opened in a glovebox and the jelly rolls were unrolled under Ar atmosphere. Fig. 1f schematically depicts the design of the double-side coated electrodes along with the dimensional characteristics measured for three cells of batch 2. For both, the anode and the cathode, an Al foil is used as the current collector. This is in contrast with another type of commercial SIB cell previously reported, where a Cu current collector was utilized for the anode as in LIB cells [28]. While the coated areas are the same size for the core- and case-facing side of the cathode, the anode coating area of the core-facing side is larger than that of the case-facing side, where approximately 68 mm of blank collector foil were found at the outer-most end of the electrode. Furthermore, the cathode current collector tab and the tab located at the outer-most range of the anode were identified as being attached to the respective electrode on the case-facing side. In contrast, the anode current collector tab at the inner-most range of the electrode is on the core-facing side of the anode. In general, the anode is longer and wider than the cathode with a total length and width of ~651 mm and ~59 mm compared to ~573 mm and ~57 mm, respectively. It is worth noting that these lengths differ significantly from the dimensions determined for the electrodes retrieved from the cells of batch 1 [32]. Indeed, total lengths of ~709 mm and ~633 mm were measured for the anode and cathode, respectively, in batch 1 [32]. However, there are no differences in terms of electrode widths between the two batches.

Regarding the electrode thicknesses, on the one hand, the same Al collector foil thickness of ~12 μm as recently reported for the electrodes from batch 1 [32] was determined for both the anode and the cathode foils for batch 2. On the other hand, a single-sided anode coating thickness of in average ~101 μm was measured for the cells of batch 2, which is more than 10 μm thicker than our previous investigation for batch 1 [32]. Overall, the anodes of both batches of SIB cells investigated in this study are thicker than those of a different type of commercial 18650 SIB cell, for which a coating thickness of 76–78 μm was determined [28]. For the single-sided cathode coating, an average thickness of ~67 μm was measured for the cells of batch 2, which is also slightly thicker than our previous results for batch 1 [32]. In this context, it is important to note that, generally, for the coating thicknesses of both electrodes, inhomogeneities were found along the electrodes and for the core- and case-facing side with high cell-to-cell variations, implying that there is still room for improvement for the overall production and quality control.

In order to identify the solvent components of the electrolyte of the commercial 18650 SIB cell, headspace GC-MS measurements were conducted on anodes, which were sealed immediately after the cell opening. The resulting chromatogram shown in Fig. S1 indicates the presence of DMC, ethyl methyl carbonate (EMC), EC, and PC. Mixtures of these carbonates are typically used as solvents in non-aqueous electrolytes for SIB cells [44,45]. On the one hand, EC, DMC, and EMC are also common components of state-of-the-art electrolytes for LIB cells [46,47]. On the other hand, PC is usually not used as a solvent for LIB cells due to its tendency to co-intercalate between the graphene layers of the graphite anode, leading to exfoliation [48]. No electrolyte additives were detected via GC-MS. However, it cannot be excluded that such components might already have reacted during formation on the electrode surface or that they were not sufficiently volatile for the available headspace method.

The DSC analysis, reported in Fig. S2 and performed on the separators retrieved from 18650 SIB cells of batch 1 and 2, shows for both batches an endothermic peak due to melting of the separator material. However, the temperature at which the melting process takes place differs for the cells of the two batches (batch 1: 165 °C, batch 2: 133 °C), likely indicating the use of different separator materials for cells of batch 1 and batch 2. The temperature of the peak of batch 1 agrees well with the melting range of polypropylene (PP), whereas it matches to polyethylene (PE) for batch 2 [49]. Both PE and PP are also typically used in LIB cells, in fact, sometimes together in multilayer separators [49–51]. The fact that the separator material was changed for batch 2, as well as the already discussed significant differences in the cell design between the cells of the investigated batches, suggests that there is an ongoing further optimization of the cell design and composition.

Fig. 2 displays the results of the morphological and structural analysis of the electrodes retrieved from the 18650 SIB cells of batch 2 in terms of cross-sectional SEM-EDX (Fig. 2a–q) and XRD (Fig. 2r and s). The cross-sectional micrographs of the anode at various magnifications (Fig. 2a–c) reveal an electrode coating composed of randomly shaped “edgy” particles that are uniformly distributed throughout the entire coating with sizes ranging from 1 μm to over 5 μm, surrounded by a blend accounting for the polymer binder and conducting carbon used for electrode manufacturing. The corresponding EDX elemental map of carbon (Fig. 2d) confirms the carbonaceous nature of the primary particles, indicating that the active material is a hard carbon, and displays lower density regions in correspondence of the surrounding blend, being in line with the presence of a conducting carbon in the coating. Likewise, the presence of sodium in the polymer binder is evidenced by the corresponding EDX map (Fig. 2e), suggesting the use of a water-soluble binding agent such as sodium carboxymethyl cellulose (CMC) [52]. The presence of oxygen is detected for both the hard carbon particles and the binder/conducting carbon mixture (Fig. 2f), as expected by the carbon terminal groups and O-bridges in the polymer binder, while the elemental maps for F (Fig. 2g) and P (Fig. 2h) suggest the decomposition of the conducting salt such as $NaPF_6$ at the electrode surface and the

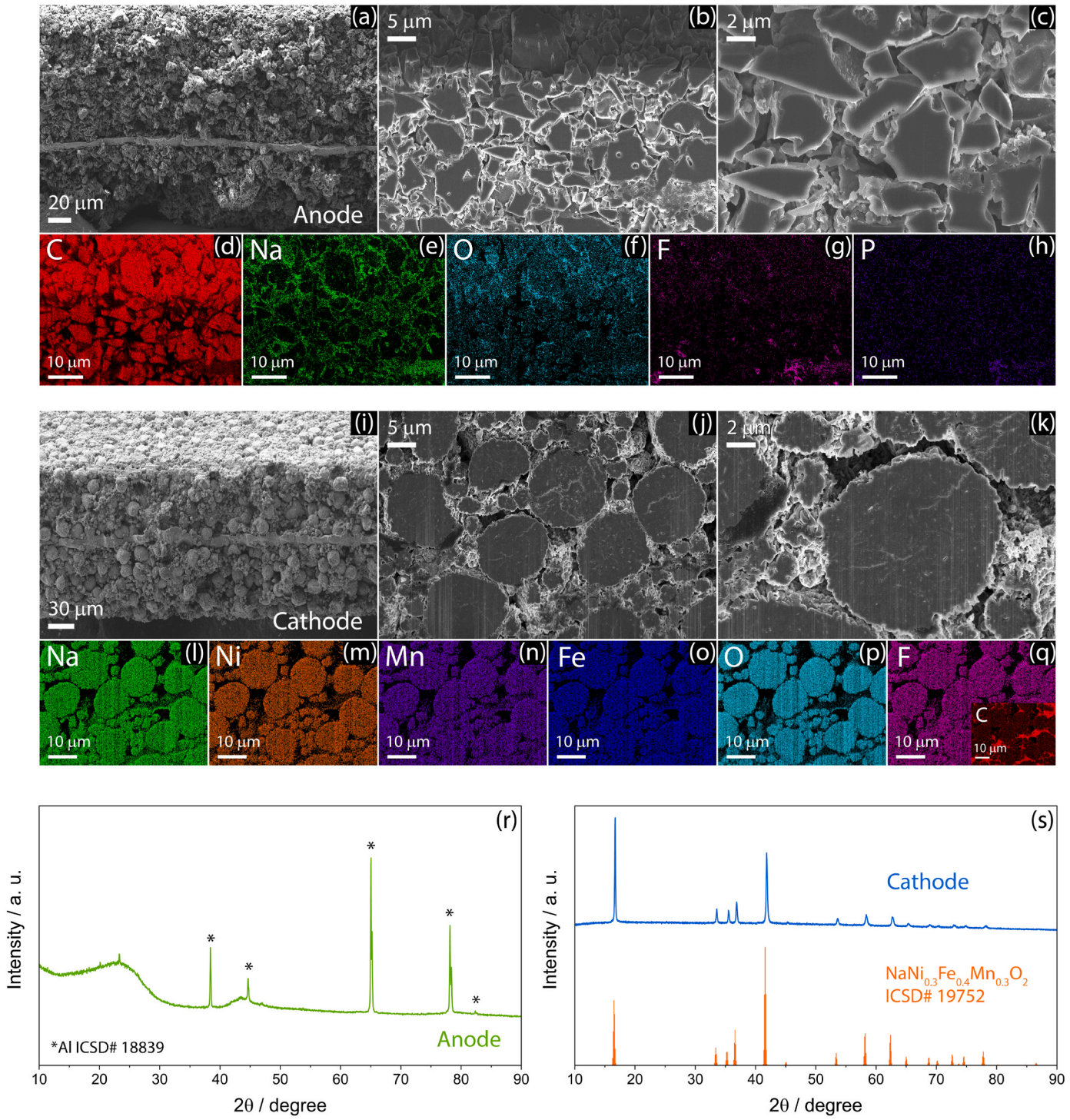


**Fig. 2.** **(a–q)** SEM-EDX analyses of the **(a–h)** anode and **(i–q)** cathode retrieved from the 18650 SIB cells. In detail: **(a-c, i-k)** SEM cross-sectional images and **(d-h, l-q)** corresponding EDX elemental maps (the EDX analyses for the cathode are reported in Table 1); **(r, s)** X-ray diffractograms of the **(r)** anode and **(s)** cathode (reference data of $NaNi_{0.3}Fe_{0.4}Mn_{0.3}O_2$ (ICSD #19752) are reported in panel **(s)** for comparison).

formation of a solid electrolyte interphase (SEI) in line with possible formation cycles performed on the SIB cell after assembly and prior to the eventual shipping to the customer [28].

The SEM micrographs acquired for the cathode (Fig. 2i–k) reveal the presence of active material particles with a spherical shape and mixed size of either ca. 2 µm or about 10 µm, surrounded by the binder/conducting carbon mixture. The related EDX elemental maps (Fig. 2l–q) show a homogenous distribution of Na (Fig. 2l), Ni (Fig. 2m), Mn (Fig. 2n), Fe (Fig. 2o) and O (Fig. 2p) within the particles, accounting for the active material with the general formula $Na_xNi_yFe_zMn_{1-y-z}O_2$ [32], as well as of F (Fig. 2q), in line with an interphase formation and/or the presence of fluorine in the binder along with a further distribution due to the ion beam cutting, while C (inset in Fig. 2q) is mainly detected in the binder/conducting carbon regions. The stoichiometric coefficients for Ni, Mn, and Fe were determined by EDX and the results are presented in Table 1, revealing an essentially equal content for the transition metals between 0.32 and 0.35, in agreement with previous surface SEM-EDX analyses [32].

**Table 1**
EDX analyses acquired on the cross-sectional SEM images shown in Fig. 2i–k and on TEM micrographs displayed in Fig. 3g related to the cathode retrieved from the 18650 SIB cell. The results are reported both in atomic concentration and as corresponding stoichiometric coefficients.

| Element | EDX on SEM (At.%) | Stoich. coeff. (SEM) | EDX on TEM (At.%) | Stoich. coeff. (TEM) |
|---|---|---|---|---|
| Ni | 7.2 | 0.33 | 9.40 | 0.32 |
| Fe | 7.5 | 0.35 | 9.86 | 0.34 |
| Mn | 6.9 | 0.32 | 10.07 | 0.34 |

Additional morphological insights into the 18650 SIB cell electrodes were obtained by surface SEM imaging, presented in Fig. S3. The micrographs confirm the uniform distribution of randomly shaped, "edgy" hard carbon particles for the anode (Figs. S3a–c) and spherical particles for the cathode, ranging from 2 μm to 10 μm (Figs. S3d–f), both being surrounded by a binder/carbon mixture. MIP measurements performed on the electrodes retrieved from the SIB cell reveal that the porosity of the anode from the pristine cell is ~35 %, whereas the cathode has a porosity of ~31 %. These porosity values are in the same range as the ones determined for a hard carbon-based anode and $Na_xNi_yFe_zMn_{1-y-z}O_2$-based cathode of another type of commercially available 18650 SIB cells investigated recently [28]. Generally, the anode porosity of the herein investigated SIB cell is higher than the porosity determined for graphite (~29 %) [53] and Si/graphite (~29 %) [33] anodes retrieved from commercial high-power LIB cells, indicating one potential approach to further enhance the energy density of SIBs. Additional SEM measurements carried out on the bare aluminum current collectors after removal of the coating layer mirror the characteristic morphology of the active materials of the two electrodes (Fig. S4). The aluminum sample obtained from the anode (Figs. S4a–c) exhibits a rough and scratched surface, while the cathode current collector (Figs. S4d–f) displays a homogenous distribution of 10 μm-sized prominences, indicating that the electrodes have been well calendared to decrease the porosity, while still being higher than for commercial LIBs.

The structural features investigated via XRD show for the anode the expected amorphous pattern typical of hard carbons (Fig. 2r), identified by two broad signals centered at around 23° and 44° corresponding to the (002) and (100) lattice spacings, respectively [54,55]. Differently, the cathode displays a well-defined crystalline pattern in line with the layered structure of $Na_xNi_yFe_zMn_{1-y-z}O_2$ (Fig. 2s), as confirmed by the reference data reported for comparison. The results of the Rietveld refinement performed on the cathode XRD pattern are depicted in Fig. S5. They show that the cathode active material structure is consistent with an O3-type layered manganese oxide, with no relevant indication of any crystallized admixture phase. The evaluation of the *a* and *c* unit cell parameters reveals values of 2.96660(4) Å and 16.0911(6) Å, respectively, leading to a corresponding volume of 122.640(5) $Å^3$ (inset in Fig. S5a). In addition, Table S1 reports the detailed crystallographic data, including atomic positions, occupancies ($a_i$), coordinates ($x$, $y$, $z$), and thermal displacement parameters ($U_{iso}$), allowing for the estimation of $Na_{0.93(1)}$ per formula unit in the active material via the analysis of the sodium occupation at the (0,0,0) position. This relevant sodium content well correlates with the stochiometric value of 0.88 for Na previously determined using inductively coupled plasma optical emission spectroscopy (ICP-OES) [32]. Moreover, the established *a* and *c* unit cell dimensions, together with the interplanar/interslab distances for the (003) and (104) planes of $d_{003} = 5.36$ Å and $d_{104} = 2.16$ Å, respectively (Fig. S5b), are in good agreement with previous investigations on O3-$NaFe_{1/3}Ni_{1/3}Mn_{1/3}O_2$ [56]. In this regard, the stochiometric value for Na is slightly lower than 1, as observed herein, potentially due to the formation cycles performed on the 18650 SIB cell before opening, justifying the higher *c* and $d_{003}$ interslab distance values expected from the pristine O3-$NaFe_{1/3}Ni_{1/3}Mn_{1/3}O_2$, as well as the decreased *a* parameter [56].

Further details on the morphology and composition of the active materials used in the 18650 SIB cells are provided in Fig. 3 by the TEM/STEM-EDX study performed on the electrode powders obtained from the coatings of the hard carbon anode and the layered oxide cathode. The TEM micrographs obtained for the anode powder (Fig. 3a and b) confirm the rather random morphology of the hard carbon particles with prevalently micrometric size. The corresponding EDX elemental maps obtained in STEM mode (Fig. 3c–f) highlight the coverage of the carbon particles by Na, O, and F, which is in line with sodium-containing polymer binder, oxygen terminal groups and F-based conducting salt as previously observed with SEM-EDX. Concerning the cathode powder, TEM reveals primary particles with a size of around 500 nm (Fig. 3g) and allows for the direct observation of the layered structure, evidencing an interlayer distance of about 5.59 Å (Fig. 3h), which is in line with the interplanar $d_{003}$ distance value detected through XRD refinement. A more precise evaluation of this parameter is additionally provided by the SAED pattern in Fig. S6, which indicates a value of 5.39 Å for the (003) planes and 2.16 Å for the (104) ones, being in very good agreement with the XRD refinement data. The EDX elemental maps (Fig. 3i–n) further corroborate the composition of the cathode active material by identifying Na, Ni, Mn, Fe and O, alongside traces of C accounting for the binder and conductive carbon, while the corresponding analyses in Table 1 confirm the equal content for the transition metals.

Further investigation was conducted by means of XPS measurements (Fig. 4), which were carried out on both anode (Fig. 4a–g) and cathode (Fig. 4h–n) after extraction from the 18650 SIB cell. Interestingly, the survey spectra show for both the hard carbon (Fig. 4a) and $Na_xNi_yFe_zMn_{1-y-z}O_2$ (Fig. 4h) electrodes the same set of signals, revealing the expected presence of Na, F, O, and C, and additionally signals of P, Cl, and N [57], indicating the formation of passivation layers with similar composition on the two electrodes. In more detail, the high-resolution spectra obtained for the anode (Fig. 4b–g) reveal contributions in the C 1s region (Fig. 4b) from C-C/C-H, C-O and C=O (likely O-C=O) bonds at 284.7 eV, 286.5 eV and 288.7 eV [58–61], respectively, which is confirmed by the O 1s signals for C=O at 531.6 eV and C-O at 533.5 eV (Fig. 4c) [62,63]. This is in line with decomposition products deriving from carbonate-based solvents used in the electrolyte solution and with the presence of a cellulose-based binder. Information on the nature of the conducting salt is provided by the F 1s (Fig. 4d) and P 2s (Fig. 4g) high-resolution spectra, that show the typical signature of deposited/decomposed $NaPF_6$ at 687.6 eV and 194.2 eV, respectively, while traces of NaF deriving from salt by-products are detected at 684.4 eV (Fig. 4d) [60,64]. In addition to the expected presence of the relevant Na 1s signal in the hard carbon electrode at 1072.7 eV (Fig. 4e), ascribable to the deposited/decomposed conducting salt and possibly to Na from the carboxymethyl cellulose binder [61], the XPS analysis reveals non-negligible contributions from C-N-based species in the N 1s region at 400.2 eV (Fig. 4f) and NaCl (Cl $2p_{3/2}$ peak at 198.2 eV, Fig. 4g) [65,66]. The presence of N and Cl suggest the use of electrolyte additives to promote the formation of beneficial passivation layers, where NaCl may derive from the decomposition of $NaClO_4$, which has relevant SEI-forming abilities in addition to the conducting properties [67]. In fact, the use of various N-based passivating species in SIBs has been previously reported [65,68].

The high-resolution spectra obtained for the cathode (Fig. 4i–n) show a similar response, where the C 1s region (Fig. 4i) displays additional signals for graphitic $sp^2$ carbon at 284.0 eV [68], likely deriving from the conducting carbon additive, and a C-F bond at 290.5 eV, indicating the use of a F-based binder such as PVdF [58]. The presence of C-O and C=O bonds is apparent in the C 1s (Fig. 4i) and O 1s (Fig. 4j) spectra, while the relative intensities differ from the anode, likely due to contributions from the electrode coating composition [62,63]. In general, the F 1s (Fig. 4k), Na 1s (Fig. 4l) and N 1s (Fig. 4m) detail spectra present a result similar to that observed for the anode, while the F 1s spectrum additionally includes a contribution from the C-F bond of the binder with the main peak at 687.5 eV [64,69]. Interestingly, the

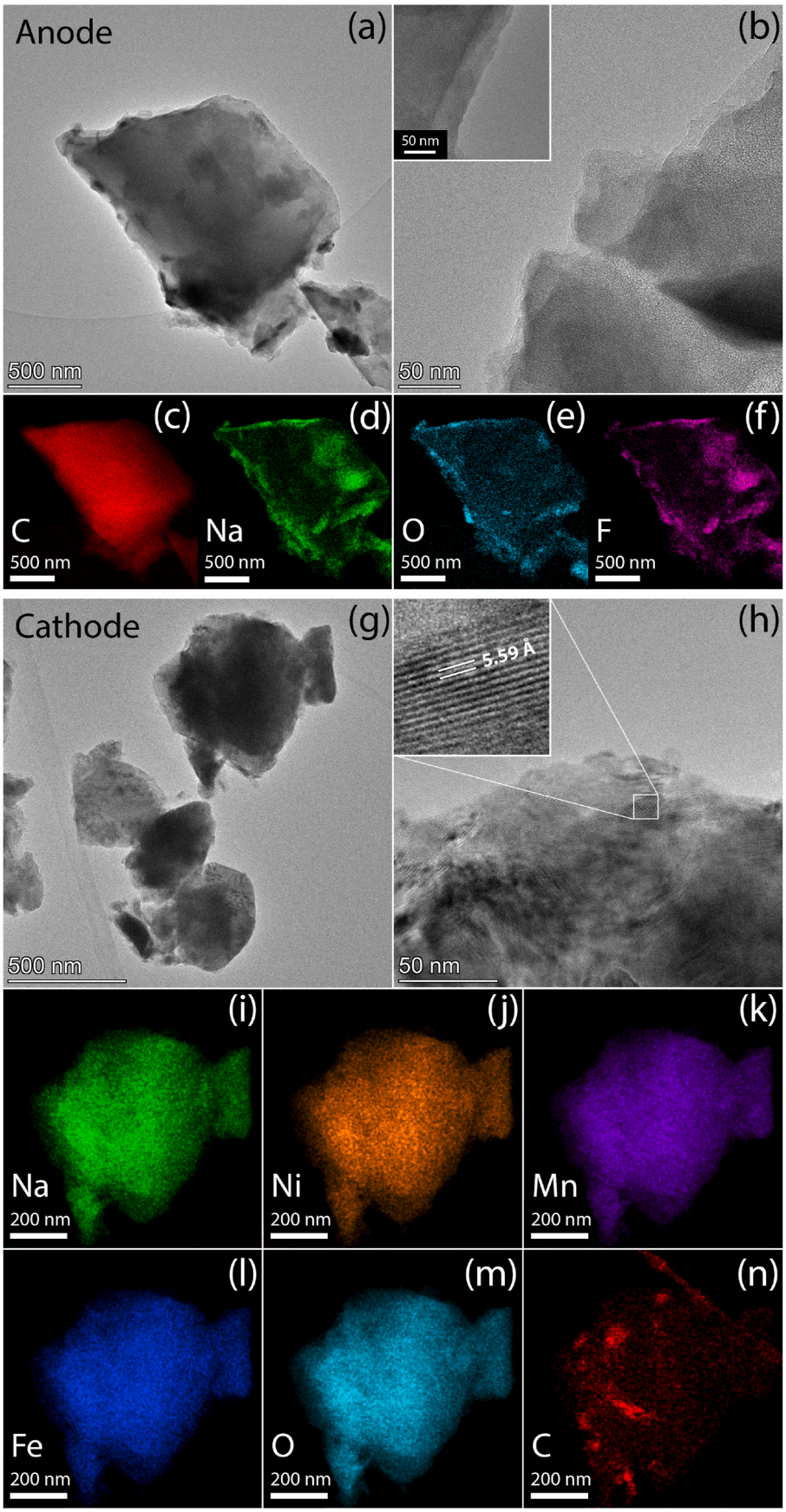


**Fig. 3.** TEM/STEM-EDX analyses of powders obtained from the **(a–f)** anode and **(g–n)** cathode retrieved from the 18650 SIB cell. In detail: **(a, b, g, h)** TEM images and **(c-f, i-n)** the corresponding EDX elemental maps (the results of the EDX analysis for the cathode are reported in Table 1).

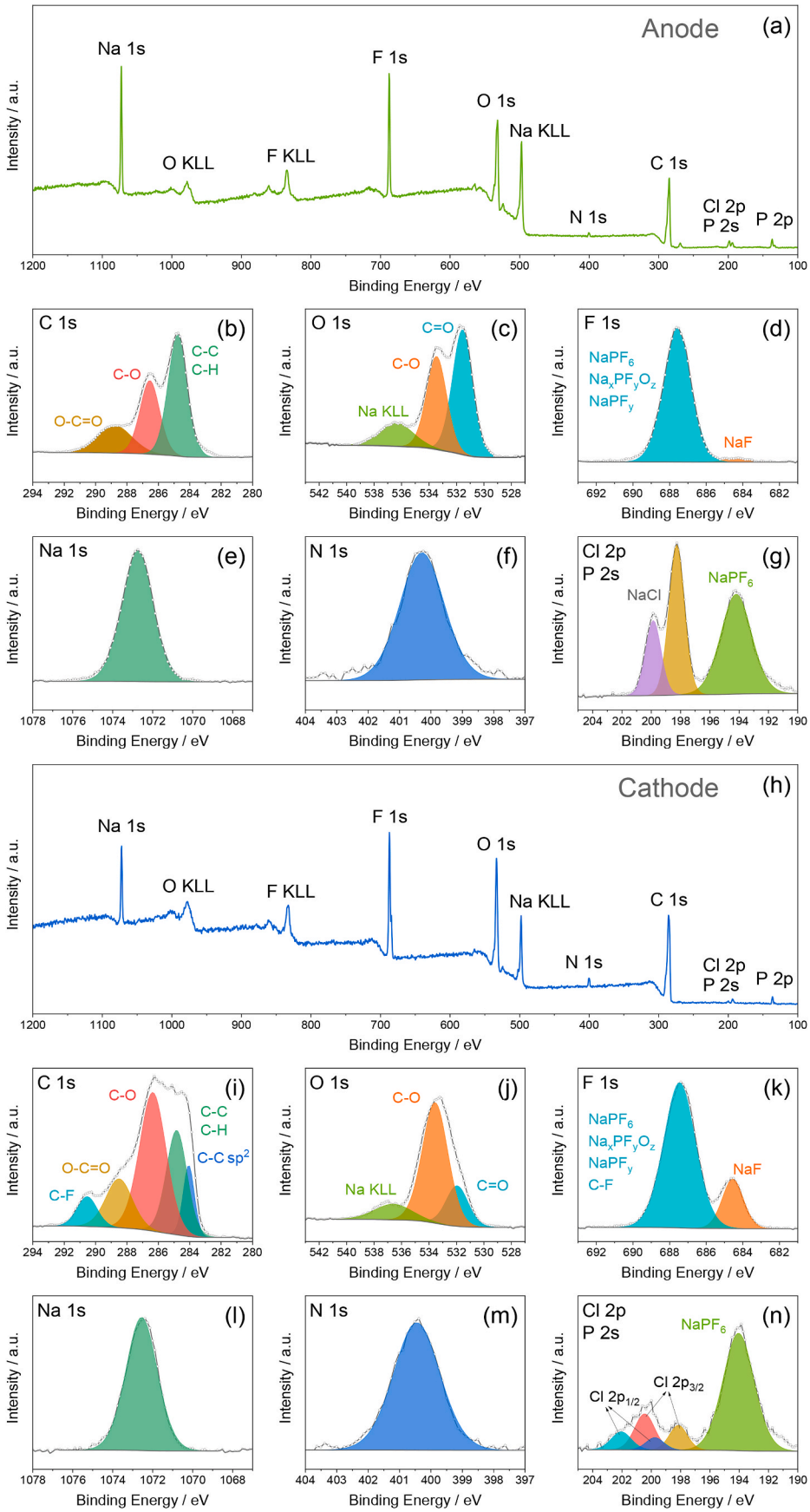


**Fig. 4.** XPS analysis of the **(a–g)** anode and **(h–n)** cathode extracted from the 18650 SIB cells. In detail: **(a, h)** survey spectra and **(b-g, i-n)** high-resolution detail spectra. Additional XPS data collected on the cathode powder are reported in Fig. S7.

spectrum of the Cl 2p/P 2s region (Fig. 4n) confirms the presence of $NaPF_6$ at 194.0 eV, and reveals at the same time a much lower intensity for the Cl 2p signals, suggesting a minor deposition/decomposition of the Cl-based additive at the outer layers of the cathode interphase. Noticeably, the absence of signals ascribable to Ni, Mn, and Fe, and to the metal-oxygen interaction in the $Na_xNi_yFe_zMn_{1-y-z}O_2$ lattice [62,69,70] indicates a relatively thick interphase being formed at the positive electrode. Thus, additional XPS analysis was performed on the cathode coating powder after fine manual grinding to expose the transition metal signals and provide further insights into the electrode composition, as displayed in Fig. S7. As expected, the survey spectrum (Fig. S7a) exhibits also the response from Fe, Mn, and Ni. The corresponding high-resolution 2p spectra of the transition metals (Figure S7b, c and d, respectively) allow for the estimation of the oxidation state, being +3 for Fe, as indicated by the main Fe $2p_{3/2}$ and $2p_{1/2}$ signals at 711.9 eV and 724.4 eV [71,72], respectively, and +4 for Mn, as indicated by the Mn $2p_{3/2}$ and $2p_{1/2}$ signals at 642.4 eV and 654.1 eV, respectively [71,73]. In addition, the Cl 2p region of the cathode coating powder (Fig. S7e) shows a notable growth of the NaCl peaks [66], suggesting a more relevant contribution of the Cl-based additive at the inner side of the passivation layer. It is worth mentioning that the Cl 2p signals related to NaCl may originate also (in part) from the decomposition of $NaClO_4$ despite the absence of the perchlorate signals [74], as reported in the literature [66].

The electrochemical activity of the hard carbon and $Na_xNi_yFe_zMn_{1-y-z}O_2$ electrodes retrieved from the 18650 SIB cell was evaluated in sodium half-cells via CV, EIS, and galvanostatic cycling (Fig. 5). The CV data recorded for the Na‖hard-carbon half-cells (Fig. 5a) shows a defined process close to 0 V vs. $Na^+/Na$ during the cathodic sweep, related to the insertion of the $Na^+$ ions into the hard carbon, followed by

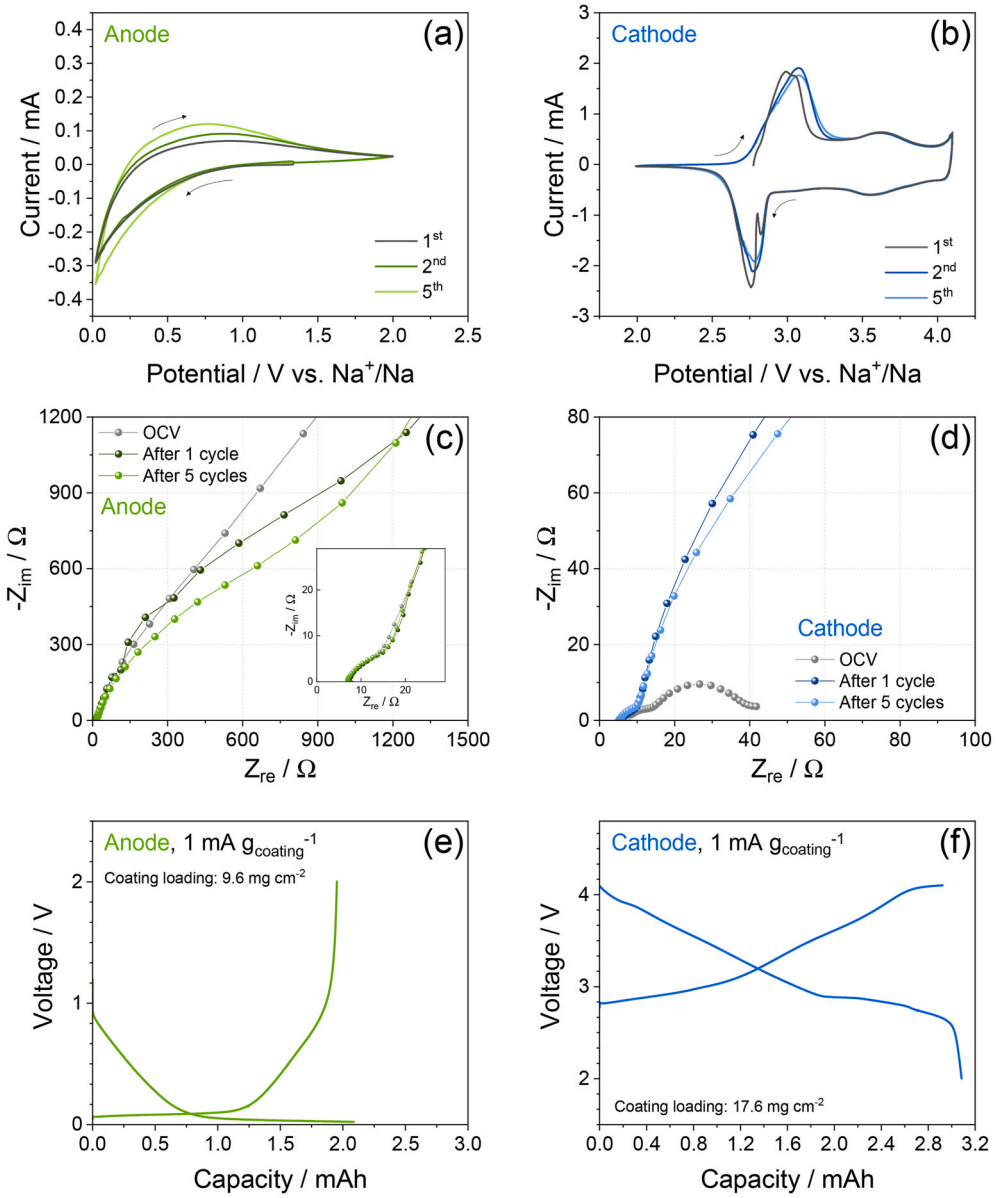


**Fig. 5.** Electrochemical investigation in sodium half-cells exploiting **(a, c, e)** the anode and **(b, d, f)** cathode retrieved from the 18650 SIB cell. In detail: **(a, b)** CV recorded at 0.1 mV $s^{-1}$ in three-electrode Swagelok cells using Na metal as additional reference electrode in the **(a)** 0.02–2.0 V vs. $Na^+/Na$ range for the anode and **(b)** 2.0–4.1 V vs. $Na^+/Na$ for the cathode; **(c, d)** Nyquist plots obtained via EIS at OCV and after 1 and 5 CV runs in the 500 kHz–100 mHz frequency range with a voltage signal amplitude of 10 mV (the inset in panel **(c)** shows a magnification); **(e, f)** galvanostatic cycling tests performed at 1 mA $g^{-1}_{coating}$ in Na half-cells using a coin-cell configuration between either **(e)** 0.02 V and 2.0 V for the anode, or **(f)** 2.0 V and 4.1 V for the cathode. The NLLS analyses of the Nyquist plots are reported in Table 2.

the deinsertion along a very broad and little pronounced peak between 0.3 and 1.0 V vs. $Na^+/Na$ upon the anodic sweep [11,67,75]. Differently, the CV data recorded for the Na||$Na_xNi_yFe_zMn_{1-y-z}O_2$ half-cells (Fig. 5b) display well defined oxidation processes at about 3.0 V and 3.6 V vs. $Na^+/Na$ in the first cycle, followed by the corresponding reduction peaks at around 3.56 V and 2.8 V vs. $Na^+/Na$. The redox couple at around 3.0 V vs. $Na^+/Na$ has been ascribed to the oxidation and reduction of $Ni^{2+}$ to $Ni^{4+}$ and vice versa, while the process between 3.5 V and 3.6 V has been associated to the $Fe^{3+}/Fe^{4+}$ redox couple [76–78]. In the subsequent cyclic sweeps, the CV data show a slight increase in potential for the nickel redox couple, and exhibit a remarkable reversibility and overlapping of the iron-related reduction/oxidation process.

Further investigation of the two different electrodes was conducted by means of EIS performed at OCV as well as after one and five cyclic sweeps (Fig. 5c and d). The resulting Nyquist plots were analyzed via the NLLS fitting method to identify the underlying resistances ($R$) and constant phase elements ($Q$). The resistance contributions include the electrolyte resistance ($R_e$), i.e., the high frequency intercept of the plot, the interphase resistance ($R_i$), i.e., the sum of the amplitudes of the high-middle frequency semicircles ($R_n$, $n = 1, 2$) arranged in parallel with the $Q_n$ constant phase elements in ($R_nQ_n$), and the resistance associated to finite-length Warburg-type $Na^+$ diffusion arranged in parallel in the ($R_wQ_w$) segment, i.e., the amplitude of the low-frequency semicircle [36,37]. The NLLS outcomes are reported in Table 2. For fitting the results obtained for the Na||hard-carbon half-cell, a $R_e(R_1Q_1)(R_2Q_2)$ equivalent circuit was chosen with an initial $R_i$ above 2300 Ω at OCV that increases to ~3000 Ω after one cycle and decreases to ~1420 Ω after five cyclic sweeps. Nonetheless, the interphase still presents a relevant resistive character eventually, indicating that the charge transfer and storage at the negative electrode might be the limiting factor for the rate capability and overall performance of the full-cells. In fact, the Na||$Na_xNi_yFe_zMn_{1-y-z}O_2$ half-cells display a very low overall impedance, with an initial $R_i$ value of only ~8 Ω, which further decreases to less than 5 Ω upon cycling (Table 2). The NLLS results well agree with the kinetics of the $Na_xNi_yFe_zMn_{1-y-z}O_2$ electrode apparent from the CV data (Fig. 5b), and show in addition a slight change in the number of ($R_nQ_n$) segments of the equivalent circuit from $R_e(R_1Q_1)(R_2Q_2)(R_wQ_w)$ at OCV to $R_e(R_1Q_1)(R_wQ_w)$ after one cycle as a result of the interphase and electrode rearrangement upon cycling, which leads to slight changes in the electrochemical process kinetics as observed also in the modification of the shape of the CV profiles from the first to the subsequent ones as mentioned earlier. It is worth noting that the width of the low-frequency semicircle attributed to the cathode in Fig. 5d (identified by the $(R_wQ_w)$ element in the equivalent circuits reported in Table 2) significantly increases after the first CV cycle, which may be due to the (repeated) sodiation of the active material or to structural rearrangements of the electrode bulk in the discharged state that hinders the diffusion of $Na^+$ ions, as previously observed in the literature [79].

Subsequently, the electrodes were briefly evaluated via galvanostatic cycling in half-cell configuration for one dis-/charge cycle at a specific current of 1 mA $g_{coating}^{-1}$ (Fig. 5e and f). The voltage profile related to the hard carbon half-cell (Fig. 5e) displays during discharge a sloping region developing from 0.90 V to 0.75 V, ascribed to the insertion of $Na^+$ ions in the carbon structure, followed by the plateau region extending down to 0.02 V, which has been assigned to the insertion of $Na^+$ ions into the hard carbon micropores [80,81], leading to a total capacity of about 2.1 mAh during discharge, and a subsequent charge capacity of around 2.0 mAh.

The voltage profile obtained for the $Na_xNi_yFe_zMn_{1-y-z}O_2$ half-cell (Fig. 5f) shows an initial sloped plateau starting from about 2.9 V, followed by a sloping region centered at around 3.3 V and a final plateau at above 4.0 V, yielding a total charge capacity of 2.9 mAh. The subsequent discharge delivers a capacity as high as 3.1 mAh. This very brief evaluation of the two different electrodes via galvanostatic cycling further confirms that the hard carbon anode appears to be the bottleneck for achieving high-rate capability and performance, while the $Na_xNi_yFe_zMn_{1-y-z}O_2$ cathode appears well engineered already.

Fig. 6 shows the results of the rate capability tests carried out on five commercial 18650 SIB full-cells. The discharge rate capability was tested during the first 24 cycles by discharging the cells three times at each individual C rate (i.e., C/10, C/5, C/3, C/2, 1C, 2C, 3C, and then again C/10 where 1C = 1.5 A). Fig. 6a compares the voltage profiles of the discharge curves of the first discharge cycle at C/10 and the last discharge at 3C. Overall, there is a good reproducibility of the data between the five tested cells. The discharge voltage curves recorded at 3C are shifted toward lower voltages compared to the discharge curves at C/10 due to higher polarization effects resulting from the higher current flow, which leads to higher overpotentials with increasing C rate [82]. An average discharge capacity of 1.56 ± 0.01 Ah is delivered by the pristine cells during the first cycle at C/10. In contrast, the average delivered capacity during the last discharge cycle at 3C is limited to about 1.45 ± 0.02 Ah. This trend is consistent with the normalized end-of-discharge capacities shown in Fig. 6b. Up to a C rate of C/3, there is only little difference observable between the capacity retention of the five different cells used for these measurements, and the discharge capacity is stable within the three cycles performed at each of the lower C rates. However, for C rates > C/2, there is a greater scattering between the normalized capacity values. Moreover, the capacity retention decreases with every additional discharge cycle. For example, at the highest C rate of 3C, an average capacity retention of ~93.4 % is reached for the first cycle, while it further decreases to ~92.7 % in the third cycle. The dropping capacity retention indicates the occurrence of significant capacity losses in this test with multiple cycles per C rate compared to our previous observation for rate capability tests with only one cycle per each C rate [32]. The significant drop in capacity observed for dis-/charge rates between 1C and 3C strongly suggests a wide room for improvement, especially in view of the maximum continuous discharge rate of 3C indicated in the producer data sheet. Although not explicitly stated by the manufacturer, this observation underlines that the investigated cell type seems to be optimized for high energy rather than high power applications. This is in line with our previous report, where we found that the specific energy of these SIBs is higher than that of previously studied $LiFePO_4$-based LIB cells optimized for high power applications [32]. Moreover, the reduced capacity retention of only 97–98 % for the C/10 control cycles at the end of the discharge rate capability test likely indicates irreversible side reactions involving electrolyte or electrode deterioration that hinder the full delivery of capacity.

Charge rate capability tests were performed after the discharge ones in the subsequent 29 cycles (cycle number 25–53), implementing control cycles at C/10 before each increase in C rate to observe possible irreversible capacity losses. In order to evaluate the fast-charging

**Table 2**
NLLS analyses performed via the Boukamp software [33,34] on the Nyquist plots reported in Fig. 5 recorded by EIS upon CV in Na half-cells exploiting either the anode or cathode extracted from the 18650 SIB cell as the working electrode.

| Electrode | Cell condition | Circuit | $R_1$ [Ω] | $R_2$ [Ω] | $R_i$ ($\sum R_n$) [Ω] | $\chi^2$ |
|---|---|---|---|---|---|---|
| Anode | OCV | $R_e(R_1Q_1)(R_2Q_2)$ | 7.6 ± 0.5 | 2331 ± 124 | 2338 ± 87 | $1 \times 10^{-4}$ |
| | After 1 cycle | $R_e(R_1Q_1)(R_2Q_2)$ | 9.7 ± 0.6 | 2093 ± 122 | 3003 ± 86 | $4 \times 10^{-4}$ |
| | After 5 cycles | $R_e(R_1Q_1)(R_2Q_2)$ | 7.7 ± 0.6 | 1413 ± 78 | 1421 ± 55 | $8 \times 10^{-4}$ |
| Cathode | OCV | $R_e(R_1Q_1)(R_2Q_2)(R_wQ_w)$ | 2.7 ± 0.2 | 5.2 ± 0.5 | 7.9 ± 0.4 | $6 \times 10^{-5}$ |
| | After 1 cycle | $R_e(R_1Q_1)(R_wQ_w)$ | 4.7 ± 0.2 | / | 4.7 ± 0.2 | $1 \times 10^{-4}$ |
| | After 5 cycles | $R_e(R_1Q_1)(R_wQ_w)$ | 4.5 ± 0.2 | / | 4.5 ± 0.2 | $2 \times 10^{-4}$ |

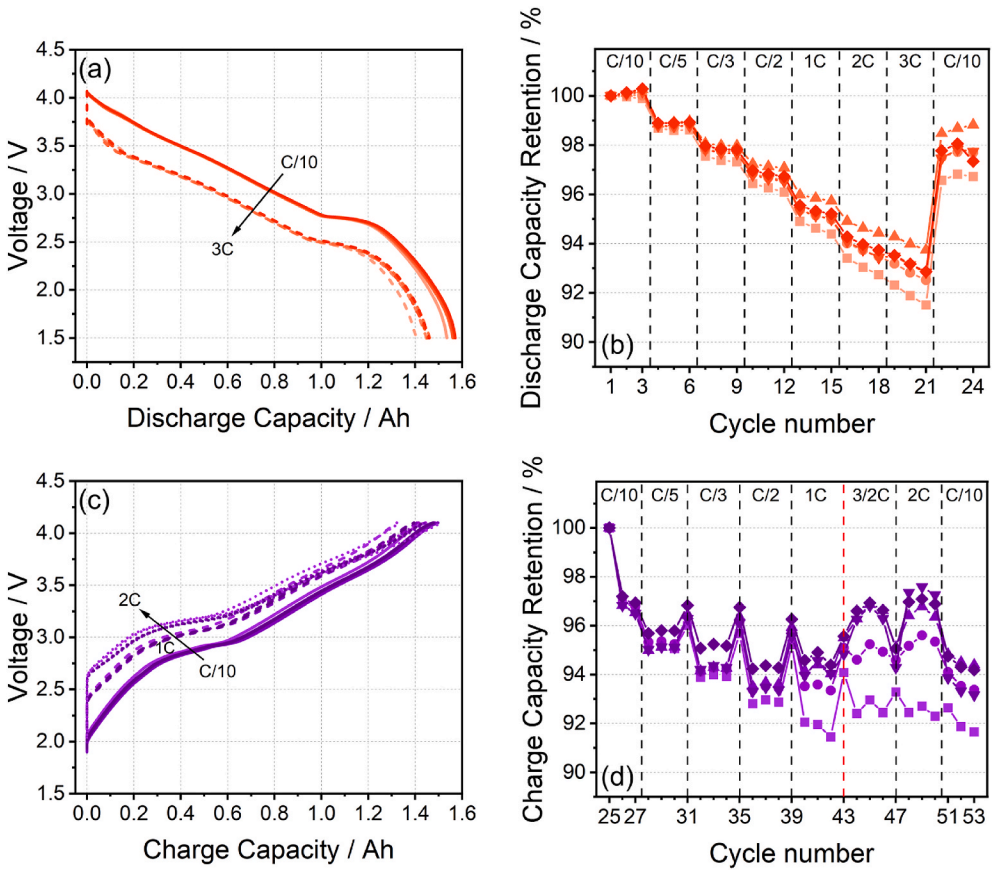


**Fig. 6.** **(a, b)** Discharge and **(c, d)** charge rate capability tests performed on five 18650 SIB cells. In detail: **(a)** comparison of the discharge voltage curves for the first discharge step at C/10 and the third discharge step at 3C; **(b)** discharge rate-dependent capacity retention trend normalized to the discharge capacity of the first cycle; **(c)** comparison of the charge voltage curves for the first charge step at C/10 and the third charge step at 1C and 2C, respectively; **(d)** charge rate-dependent capacity retention trend normalized to the charge capacity of the first cycle.

capability of the 18650 SIB cells, even higher C rates than the maximum allowed C rate of 1C mentioned in the data sheet from the manufacturer were tested. The corresponding charge voltage curves for the first cycle at C/10, as well as for the last cycles at 1C and 2C, are characterized once more by a good data reproducibility for five cells, as depicted in Fig. 6c. Similar to the discharge curves (Fig. 6a), higher overpotentials are observed for the charge profiles for an increasing C rate.

The capacity retention trends obtained from the charge rate capability tests are shown in Fig. 6d. In this case, the end-of-charge capacities are normalized to the charge capacity obtained from the first cycle performed at the lowest C rate of C/10. In general, the scattering of the charge capacity retention is higher than that of the discharge counterparts. In particular, at C rates exceeding the mentioned maximum C rate of 1C allowed by the manufacturer's data sheet, the electrochemical performance of the five tested cells notably differs. Remarkably, a significant capacity decrease is observed between the first and the second charge cycle at C/10, which might result from a loss of cyclable $Na^+$-ions due to Na deposition taking place on the hard carbon surface during charge. In the subsequent C/10 control cycles before the maximum charge rate is exceeded, the average charge capacity retention is only slightly further reduced, suggesting that only minor capacity losses are occurring. However, when the 18650 SIB cells are charged at C rates higher than 1C, the capacity retention suddenly increases again for 3 of the 5 tested cells, indicating that again more $Na^+$ ions can be inserted into the anode structure. Nevertheless, at the same time the capacity retention drops significantly in the intermediate and final C/10 charging steps, indicating a rapid aging of the cells during fast-charging, possibly due to Na deposition and subsequent reactions of Na metal with electrolyte, similar to the Li deposition in Li-ion cells [83,84].

## 4. Conclusions

Commercial 18650 SIB cells have been thoroughly analyzed in terms of both design/dimensional parameters, performance of the full-cells, and evaluation of the physicochemical and electrochemical properties of the anode and cathode separately. The CT analysis performed on pristine 18650 SIB cells revealed no manufacturing-related defects and a jelly roll with 18.6 windings. Dimensional evaluations of the electrode design obtained by cell opening, as well as the DSC analysis carried out on the separator material, showed significant differences between the cells of the two production batches investigated. GC-MS measurements indicated the presence of DMC, EMC, EC, and PC as solvent components in the electrolyte of the commercial 18650 SIB cell. The observed cell design is very similar to that of LIB cells, supporting the often-mentioned claim that SIB cells can be regarded as drop-in technology. Electron microscopy including SEM and TEM both coupled with EDX revealed the use of a hard carbon material for the anode composed of randomly shaped "edgy" particles with a size ranging from 1 μm to 5 μm. The cathode analysis confirmed the use of a layered oxide active material with particle size ranging from 2 μm to 10 μm, with Ni, Mn, and Fe being present in the same concentration, in line with the $Na_xNi_yFe_zMn_{1-y-z}O_2$ formula. XRD experiments confirmed the disordered structure of the hard carbon, while the Rietveld refinement of the $Na_xNi_yFe_zMn_{1-y-z}O_2$ pattern allowed for the determination of the O3-type structure and a sodium content close to 1 ($Na_{0.93}$). XPS analyses indicated the possible use of Cl- and N-based additives in the electrolyte, while additional XPS performed on the cathode coating powder led to the determination of the oxidation states of +3 and + 4 for Fe and Mn, respectively. CV coupled with EIS was performed on three-electrode Na half-cells to

assess the respective electrochemical features of the two different electrodes. The experiments displayed sluggish kinetics for the hard carbon electrode, while the $Na_xNi_yFe_zMn_{1-y-z}O_2$ cathode exhibits a very low resistance and excellent reversibility. The evaluation of the performance of the commercial 18650 SIB full-cells by rate capability tests revealed irreversible capacity losses occurring in particular at higher C rates, underlying that the herein investigated cell type is more suitable for high-energy than high-power applications.

## CRediT authorship contribution statement

**Vittorio Marangon:** Writing – original draft, Investigation, Formal analysis, Data curation, Conceptualization. **Katharina Bischof:** Writing – original draft, Investigation, Formal analysis, Data curation. **Aislim Aracil Regalado:** Investigation, Formal analysis, Data curation. **Miriam Keppeler:** Investigation, Formal analysis, Data curation. **Mariam Pogosova:** Writing – review & editing, Investigation, Formal analysis, Data curation. **Mintao Wan:** Investigation, Formal analysis, Data curation. **Jaehoon Choi:** Investigation, Formal analysis, Data curation. **Simon Fleischmann:** Writing – review & editing, Supervision, Investigation. **Thomas Diemant:** Writing – review & editing, Investigation, Formal analysis, Data curation. **Margret Wohlfahrt-Mehrens:** Writing – review & editing, Supervision, Funding acquisition. **Markus Hölzle:** Writing – review & editing, Supervision, Resources, Funding acquisition. **Thomas Waldmann:** Writing – review & editing, Writing – original draft, Supervision, Methodology, Investigation, Formal analysis, Conceptualization. **Dominic Bresser:** Writing – review & editing, Supervision, Resources, Methodology, Investigation, Funding acquisition, Conceptualization.

## Declaration of competing interest

The authors declare that they have no known competing financial interests or personal relationships that could have appeared to influence the work reported in this paper.

## Acknowledgements

V.M., M.P., and D.B. would like to acknowledge financial support from the Ministry of Economics, Labor and Tourism in Baden-Wuerttemberg (Ministerium für Wirtschaft, Arbeit und Tourismus Baden-Württemberg) within the frame of the PRONTO project (WM34-42-57/19) as well as from the Helmholtz Association. K.B., A.A.R., M.K., M.W.-M, M.H., and T.W. gratefully acknowledge ZSW for financial support. The authors would like to thank P. Sichler (ZSW) for DSC and GC-MS measurements.

## Appendix A. Supplementary data

Supplementary data to this article can be found online at https://doi.org/10.1016/j.jpowsour.2025.236496.

## Data availability

Data will be made available on request.

## References

[1] E. Goikolea, V. Palomares, S. Wang, I.R. de Larramendi, X. Guo, G. Wang, T. Rojo, Na-Ion batteries—approaching old and new challenges, Adv. Energy Mater. 10 (2020) 2002055, https://doi.org/10.1002/aenm.202002055.
[2] C. Delmas, Sodium and sodium-ion batteries: 50 Years of research, Adv. Energy Mater. 8 (2018) 1703137, https://doi.org/10.1002/aenm.201703137.
[3] A. Innocenti, D. Bresser, J. Garche, S. Passerini, A critical discussion of the current availability of lithium and zinc for use in batteries, Nat. Commun. 15 (2024) 4068, https://doi.org/10.1038/s41467-024-48368-0.
[4] Y. Tian, G. Zeng, A. Rutt, T. Shi, H. Kim, J. Wang, J. Koettgen, Y. Sun, B. Ouyang, T. Chen, Z. Lun, Z. Rong, K. Persson, G. Ceder, Promises and challenges of next-generation "beyond Li-ion" batteries for electric vehicles and grid decarbonization, Chem Rev 121 (2021) 1623–1669, https://doi.org/10.1021/acs.chemrev.0c00767.
[5] G. Calvo, A. Valero, Strategic mineral resources: availability and future estimations for the renewable energy sector, Environ Dev 41 (2022) 100640, https://doi.org/10.1016/j.envdev.2021.100640.
[6] A. Valero, A. Valero, G. Calvo, A. Ortego, Material bottlenecks in the future development of green technologies, Renew. Sustain. Energy Rev. 93 (2018) 178–200, https://doi.org/10.1016/j.rser.2018.05.041.
[7] N. Yabuuchi, K. Kubota, M. Dahbi, S. Komaba, Research development on sodium-ion batteries, Chem Rev 114 (2014) 11636–11682, https://doi.org/10.1021/cr500192f.
[8] J. Cui, A. Wang, G. Li, D. Wang, D. Shu, A. Dong, G. Zhu, J. Luo, B. Sun, Composite sodium metal anodes for practical applications, J Mater Chem A Mater 8 (2020) 15399–15416, https://doi.org/10.1039/D0TA02469D.
[9] A. Innocenti, S. Beringer, S. Passerini, Cost and performance analysis as a valuable tool for battery material research, Nat. Rev. Mater. 9 (2024) 347–357, https://doi.org/10.1038/s41578-024-00657-2.
[10] M. Baumann, M. Häringer, M. Schmidt, L. Schneider, J.F. Peters, W. Bauer, J. R. Binder, M. Weil, Prospective sustainability screening of sodium-ion battery cathode materials, Adv. Energy Mater. 12 (2022) 2202636, https://doi.org/10.1002/aenm.202202636.
[11] H. Moon, M. Zarrabeitia, E. Frank, O. Böse, M. Enterría, D. Saurel, I. Hasa, S. Passerini, Assessing the reactivity of hard carbon anodes: linking material properties with electrochemical response upon sodium- and lithium-ion storage, Batter Supercaps 4 (2021) 960–977, https://doi.org/10.1002/batt.202000322.
[12] W. Lv, F. Wen, J. Xiang, J. Zhao, L. Li, L. Wang, Z. Liu, Y. Tian, Peanut shell derived hard carbon as ultralong cycling anodes for lithium and sodium batteries, Electrochim. Acta 176 (2015) 533–541, https://doi.org/10.1016/j.electacta.2015.07.059.
[13] H. Moon, A. Innocenti, H. Liu, H. Zhang, M. Weil, M. Zarrabeitia, S. Passerini, Biowaste-Derived hard carbon anodes through a sustainable and cost-effective synthesis process for sodium-ion batteries, ChemSusChem 16 (2023) e202201713, https://doi.org/10.1002/cssc.202201713.
[14] F. Wang, T. Zhang, F. Ran, Insights into sodium-ion batteries through plateau and slope regions in cyclic voltammetry by tailoring bacterial cellulose precursors, Electrochim. Acta 441 (2023) 141770, https://doi.org/10.1016/j.electacta.2022.141770.
[15] Y. Chen, F. Li, Z. Guo, Z. Song, Y. Lin, W. Lin, L. Zheng, Z. Huang, Z. Hong, M.-M. Titirici, Sustainable and scalable fabrication of high-performance hard carbon anode for Na-ion battery, J. Power Sources 557 (2023) 232534, https://doi.org/10.1016/j.jpowsour.2022.232534.
[16] Y. Leng, S. Dong, Z. Chen, Y. Sun, Q. Xu, L. Ma, X. He, C. Hai, Y. Zhou, Preparation of high-performance anode materials for sodium-ion batteries using bamboo waste: achieving resource recycling, J. Power Sources 613 (2024) 234826, https://doi.org/10.1016/j.jpowsour.2024.234826.
[17] M. Kalibek, L. Rakhymbay, Z. Zhakiyeva, Z. Bakenov, S.-T. Myung, A. Konarov, From food waste to high-capacity hard carbon for rechargeable sodium-ion batteries, Carbon Resources Conversion 7 (2024) 100225, https://doi.org/10.1016/j.crcon.2024.100225.
[18] L. Rakhymbay, N. Bazybek, K. Kudaibergenov, S.-T. Myung, Z. Bakenov, A. Konarov, Present development and future perspectives on biowaste-derived hard carbon anodes for room temperature sodium-ion batteries, J. Power Sources 602 (2024) 234347, https://doi.org/10.1016/j.jpowsour.2024.234347.
[19] Z.-X. Huang, Z.-Y. Gu, Y.-L. Heng, E. Huixiang Ang, H.-B. Geng, X.-L. Wu, Advanced layered oxide cathodes for sodium/potassium-ion batteries: development, challenges and prospects, Chem. Eng. J. 452 (2023) 139438, https://doi.org/10.1016/j.cej.2022.139438.
[20] X. Zhang, C. Xu, Y. Bai, J. Zhao, $NaVPO_4X$ (X = O, F) as cathodes for advanced high-energy Na-ion batteries, Chem. Eng. J. 491 (2024) 152147, https://doi.org/10.1016/j.cej.2024.152147.
[21] L. Minnetti, L. Sbrascini, A. Staffolani, V. Marangon, F. Nobili, J. Hassoun, Unravelling the ion transport and the interphase properties of a mixed olivine cathode for Na-ion battery, J. Energy Chem. 96 (2024) 300–317, https://doi.org/10.1016/j.jechem.2024.04.028.
[22] W. Shu, J. Li, G. Zhang, J. Meng, X. Wang, L. Mai, Progress on transition metal ions dissolution suppression strategies in prussian blue analogs for aqueous sodium-/potassium-ion batteries, Nano-Micro Lett. 16 (2024) 128, https://doi.org/10.1007/s40820-024-01355-y.
[23] L.H.B. Nguyen, P.S. Camacho, J. Fondard, D. Carlier, L. Croguennec, M.R. Palacin, A. Ponrouch, C. Courrèges, R. Dedryvère, K. Trad, C. Jordy, S. Genies, Y. Reynier, L. Simonin, First 18650-format Na-ion cells aging investigation: a degradation mechanism study, J. Power Sources 529 (2022) 231253, https://doi.org/10.1016/j.jpowsour.2022.231253.
[24] T. Broux, F. Fauth, N. Hall, Y. Chatillon, M. Bianchini, T. Bamine, J. Leriche, E. Suard, D. Carlier, Y. Reynier, L. Simonin, C. Masquelier, L. Croguennec, High rate performance for carbon-coated $Na_3V_2(PO_4)_2F_3$ in Na-ion batteries, Small Methods 3 (2019) 1800215, https://doi.org/10.1002/smtd.201800215.
[25] L.U. Subasinghe, G. Satyanarayana Reddy, A. Rudola, P. Balaya, Analysis of heat generation and impedance characteristics of prussian blue analogue cathode-based 18650-type sodium-ion cells, J. Electrochem. Soc. 167 (2020) 110504, https://doi.org/10.1149/1945-7111/ab9ee9.
[26] Q. Zhou, Y. Li, F. Tang, K. Li, X. Rong, Y. Lu, L. Chen, Y.-S. Hu, Thermal stability of high power 26650-type cylindrical Na-ion batteries, Chin. Phys. Lett. 38 (2021) 076501, https://doi.org/10.1088/0256-307X/38/7/076501.

[27] M. He, A.E.L. Mejdoubi, D. Chartouni, M. Morcrette, P. Troendle, R. Castiglioni, High power NVPF/HC-based sodium-ion batteries, J. Power Sources 588 (2023) 233741, https://doi.org/10.1016/j.jpowsour.2023.233741.
[28] H. Laufen, S. Klick, H. Ditler, K.L. Quade, A. Mikitisin, A. Blömeke, M. Schütte, D. Wasylowski, M. Sonnet, L. Henrich, A. Schwedt, G. Stahl, F. Ringbeck, J. Mayer, D.U. Sauer, Multi-method characterization of a commercial 1.2 Ah sodium-ion battery cell indicates drop-in potential, Cell Rep Phys Sci 5 (2024) 101945, https://doi.org/10.1016/j.xcrp.2024.101945.
[29] M. Schütte, H. Laufen, D. Luder, H. Ditler, J. Kern, S. Klick, M. Junker, G. Stahl, F. Frie, D.U. Sauer, First full cell parameterization of a commercial layered oxide/hard carbon sodium-ion 18650 battery cell for a physico-chemical model, J. Energy Storage 107 (2025) 114931, https://doi.org/10.1016/j.est.2024.114931.
[30] S. Klick, H. Laufen, M. Schütte, B. Qian, K.L. Quade, C. Rahe, M. Dubarry, D. U. Sauer, Failure Mode and Degradation Analysis of a Commercial Sodium-Ion Battery with Severe Gassing Issue, Batter Supercaps, 2025 e202400546, https://doi.org/10.1002/batt.202400546.
[31] F.A. Dorau, A. Sommer, J. Koloch, R. Röß-Ohlenroth, M. Schreiber, M. Neuner, K. Abo Gamra, Y. Lin, J. Schöberl, P. Bilfinger, S. Grabmann, B. Stumper, L. Katzenmeier, M. Lienkamp, R. Daub, Comprehensive analysis of commercial sodium-ion batteries: structural and electrochemical insights, J. Electrochem. Soc. 171 (2024) 090521, https://doi.org/10.1149/1945-7111/ad7765.
[32] K. Bischof, V. Marangon, M. Kasper, A. Aracil Regalado, M. Wohlfahrt-Mehrens, M. Hölzle, D. Bresser, T. Waldmann, Evaluation of commercial 18650 and 26700 sodium-ion cells and comparison with well-established lithium-ion cells, Journal of Power Sources Advances 27 (2024) 100148, https://doi.org/10.1016/j.powera.2024.100148.
[33] M. Flügel, K. Richter, M. Wohlfahrt-Mehrens, T. Waldmann, Detection of Li deposition on Si/graphite anodes from commercial Li-ion cells: a post-mortem GD-OES depth profiling study, J. Electrochem. Soc. 169 (2022) 050533, https://doi.org/10.1149/1945-7111/ac70af.
[34] J.B. Quinn, T. Waldmann, K. Richter, M. Kasper, M. Wohlfahrt-Mehrens, Energy density of cylindrical Li-ion cells: a comparison of commercial 18650 to the 21700 cells, J. Electrochem. Soc. 165 (2018) A3284–A3291, https://doi.org/10.1149/2.0281814jes.
[35] V. Petříček, L. Palatinus, J. Plášil, M. Dušek, Jana2020 – a new version of the crystallographic computing system Jana, Z. Kristallogr. Cryst. Mater. 238 (2023) 271–282, https://doi.org/10.1515/zkri-2023-0005.
[36] B. Boukamp, A Nonlinear Least Squares Fit procedure for analysis of immittance data of electrochemical systems, Solid State Ion 20 (1986) 31–44, https://doi.org/10.1016/0167-2738(86)90031-7.
[37] B. Boukamp, A package for impedance/admittance data analysis, Solid State Ion 18–19 (1986) 136–140, https://doi.org/10.1016/0167-2738(86)90100-1.
[38] M.J. Lain, J. Brandon, E. Kendrick, Design strategies for high power vs. High energy lithium ion cells, Batteries 5 (2019) 64, https://doi.org/10.3390/batteries5040064.
[39] J. Sturm, A. Frank, A. Rheinfeld, S.V. Erhard, A. Jossen, Impact of electrode and cell design on fast charging capabilities of cylindrical lithium-ion batteries, J. Electrochem. Soc. 167 (2020) 130505, https://doi.org/10.1149/1945-7111/abb40c.
[40] T. Waldmann, R.-G. Scurtu, D. Brändle, M. Wohlfahrt-Mehrens, Effects of tab design in 21700 Li-ion cells: improvements of cell impedance, rate capability, and cycling aging, Energy Technol. 11 (2023) 2200583, https://doi.org/10.1002/ente.202200583.
[41] T. Waldmann, R.-G. Scurtu, K. Richter, M. Wohlfahrt-Mehrens, 18650 vs. 21700 Li-ion cells – a direct comparison of electrochemical, thermal, and geometrical properties, J. Power Sources 472 (2020) 228614, https://doi.org/10.1016/j.jpowsour.2020.228614.
[42] A. Pfrang, A. Kersys, A. Kriston, D.U. Sauer, C. Rahe, S. Käbitz, E. Figgemeier, Long-term cycling induced jelly roll deformation in commercial 18650 cells, J. Power Sources 392 (2018) 168–175, https://doi.org/10.1016/j.jpowsour.2018.03.065.
[43] P. Berg, M. Spielbauer, M. Tillinger, M. Merkel, M. Schoenfuss, O. Bohlen, A. Jossen, Durability of lithium-ion 18650 cells under random vibration load with respect to the inner cell design, J. Energy Storage 31 (2020) 101499, https://doi.org/10.1016/j.est.2020.101499.
[44] A. Ponrouch, D. Monti, A. Boschin, B. Steen, P. Johansson, M.R. Palacín, Non-aqueous electrolytes for sodium-ion batteries, J Mater Chem A Mater 3 (2015) 22–42, https://doi.org/10.1039/C4TA04428B.
[45] K. Vignarooban, R. Kushagra, A. Elango, P. Badami, B.-E. Mellander, X. Xu, T. G. Tucker, C. Nam, A.M. Kannan, Current trends and future challenges of electrolytes for sodium-ion batteries, Int. J. Hydrogen Energy 41 (2016) 2829–2846, https://doi.org/10.1016/j.ijhydene.2015.12.090.
[46] K. Xu, Nonaqueous liquid electrolytes for lithium-based rechargeable batteries, Chem Rev 104 (2004) 4303–4418, https://doi.org/10.1021/cr030203g.
[47] J. Kalhoff, G.G. Eshetu, D. Bresser, S. Passerini, Safer electrolytes for lithium-ion batteries: state of the art and perspectives, ChemSusChem 8 (2015) 2154–2175, https://doi.org/10.1002/cssc.201500284.
[48] R. Fong, U. von Sacken, J.R. Dahn, Studies of lithium intercalation into carbons using nonaqueous electrochemical cells, J. Electrochem. Soc. 137 (1990) 2009–2013, https://doi.org/10.1149/1.2086855.
[49] G. Venugopal, J. Moore, J. Howard, S. Pendalwar, Characterization of microporous separators for lithium-ion batteries, J. Power Sources 77 (1999) 34–41, https://doi.org/10.1016/S0378-7753(98)00168-2.
[50] C.J. Weber, S. Geiger, S. Falusi, M. Roth, Material review of Li ion battery separators (2014) 66, https://doi.org/10.1063/1.4878480, 81.
[51] S. Luiso, P. Fedkiw, Lithium-ion battery separators: recent developments and state of art, Curr. Opin. Electrochem. 20 (2020) 99–107, https://doi.org/10.1016/j.coelec.2020.05.011.
[52] F. Jeschull, M.J. Lacey, D. Brandell, Functional binders as graphite exfoliation suppressants in aggressive electrolytes for lithium-ion batteries, Electrochim. Acta 175 (2015) 141–150, https://doi.org/10.1016/j.electacta.2015.03.072.
[53] J. Schmalstieg, C. Rahe, M. Ecker, D.U. Sauer, Full cell parameterization of a high-power lithium-ion battery for a physico-chemical model: Part I. Physical and electrochemical parameters, J. Electrochem. Soc. 165 (2018) A3799–A3810, https://doi.org/10.1149/2.0321816jes.
[54] V. Velez, G. Ramos-Sánchez, B. Lopez, L. Lartundo-Rojas, I. González, L. Sierra, Synthesis of novel hard mesoporous carbons and their applications as anodes for Li and Na ion batteries, Carbon N Y 147 (2019) 214–226, https://doi.org/10.1016/j.carbon.2019.02.083.
[55] L. Sbrascini, A. Staffolani, L. Bottoni, H. Darjazi, L. Minnetti, M. Minicucci, F. Nobili, Structural and interfacial characterization of a sustainable Si/hard carbon composite anode for lithium-ion batteries, ACS Appl. Mater. Interfaces (2022) 33257–33273, https://doi.org/10.1021/acsami.2c07888.
[56] V.A. Shevchenko, I.S. Glazkova, D.A. Novichkov, I. Skvortsova, A.V. Sobolev, A. M. Abakumov, I.A. Presniakov, O.A. Drozhzhin, E.V. Antipov, Competition between the Ni and Fe redox in the O3-$NaNi_{1/3}Fe_{1/3}Mn_{1/3}O_2$ cathode material for Na-ion batteries, Chem. Mater. 35 (2023) 4015–4025, https://doi.org/10.1021/acs.chemmater.3c00338.
[57] J.F. Moulder, W.F. Stickle, P.E. Sobol, K.D. Bomben, Handbook of X-Ray Photoelectron Spectroscopy, second, Perkin-Elmer Corporation, Eden Prairie, MN, 1992.
[58] B. Qin, M. Zarrabeitia, A. Hoefling, Z. Jusys, X. Liu, J. Tübke, R.J. Behm, G. Cui, A. Varzi, S. Passerini, A unique polymer-inorganic cathode-electrolyte-interphase (CEI) boosts high-performance $Na_3V_2(PO_4)_2F_3$ batteries in ether electrolytes, J. Power Sources 560 (2023) 232630, https://doi.org/10.1016/j.jpowsour.2023.232630.
[59] M. Li, M. Floetenmeyer, E. Bryant, E. Cooper, S. Tao, R. Knibbe, Study of Na deposition formation in mixed ethylene: propylene carbonate electrolytes by inert/cryoelectron microscopy, ACS Appl. Mater. Interfaces 15 (2023) 53333–53341, https://doi.org/10.1021/acsami.3c09442.
[60] G.G. Eshetu, T. Diemant, M. Hekmatfar, S. Grugeon, R.J. Behm, S. Laruelle, M. Armand, S. Passerini, Impact of the electrolyte salt anion on the solid electrolyte interphase formation in sodium ion batteries, Nano Energy 55 (2019) 327–340, https://doi.org/10.1016/j.nanoen.2018.10.040.
[61] L.A. Ma, A. Buckel, A. Hofmann, L. Nyholm, R. Younesi, Fundamental understanding and quantification of capacity losses involving the negative electrode in sodium-ion batteries, Adv. Sci. 11 (2024) 2306771, https://doi.org/10.1002/advs.202306771.
[62] Q. Li, G. Li, C. Fu, D. Luo, J. Fan, J. Zheng, D. Xie, L. Li, A study on storage characteristics of pristine Li-rich layered oxide $Li_{1.20}Mn_{0.54}Co_{0.13}Ni_{0.13}O_2$: effect of storage temperature and duration, Electrochim. Acta 154 (2015) 249–258, https://doi.org/10.1016/j.electacta.2014.12.071.
[63] W. Li, Z. Yao, S. Zhang, X. Wang, X. Xia, C. Gu, J. Tu, Exploring the stability effect of the Co-substituted P2-$Na_{0.67}[Mn_{0.67}Ni_{0.33}]O_2$ cathode for liquid- and solid-state sodium-ion batteries, ACS Appl. Mater. Interfaces 12 (2020) 41477–41484, https://doi.org/10.1021/acsami.0c11375.
[64] Y. Lee, J. Lee, H. Kim, K. Kang, N.-S. Choi, Highly stable linear carbonate-containing electrolytes with fluoroethylene carbonate for high-performance cathodes in sodium-ion batteries, J. Power Sources 320 (2016) 49–58, https://doi.org/10.1016/j.jpowsour.2016.04.070.
[65] X. Song, T. Meng, Y. Deng, A. Gao, J. Nan, D. Shu, F. Yi, The effects of the functional electrolyte additive on the cathode material $Na_{0.76}Ni_{0.3}Fe_{0.4}Mn_{0.3}O_2$ for sodium-ion batteries, Electrochim. Acta 281 (2018) 370–377, https://doi.org/10.1016/j.electacta.2018.05.185.
[66] J. Zhang, Z. Meng, D. Yang, K. Song, L. Mi, Y. Zhai, X. Guan, W. Chen, Enhanced interfacial compatibility of FeS@N,S-C anode with ester-based electrolyte enables stable sodium-ion full cells, J. Energy Chem. 68 (2022) 27–34, https://doi.org/10.1016/j.jechem.2021.11.033.
[67] V. Marangon, E. Barcaro, F. De Boni, M. Prato, D. Bresser, J. Hassoun, Effective liquid electrolytes for enabling room-temperature sodium–sulfur batteries, Adv Sustain Syst (2024) 2400268, https://doi.org/10.1002/adsu.202400268.
[68] N. Karimi, M. Zarrabeitia, H. Geaney, K.M. Ryan, B. Iliev, T.J.S. Schubert, A. Varzi, S. Passerini, Stable cycling of Si nanowire electrodes in fluorine-free cyano-based ionic liquid electrolytes enabled by vinylene carbonate as SEI-forming additive, J. Power Sources 558 (2023) 232621, https://doi.org/10.1016/j.jpowsour.2022.232621.
[69] D. Di Lecce, V. Marangon, M. Isaacs, R. Palgrave, P.R. Shearing, J. Hassoun, Degradation of layered oxide cathode in a sodium battery: a detailed investigation by X-ray tomography at the nanoscale, Small Methods 5 (2021) 2100596, https://doi.org/10.1002/smtd.202100596.
[70] S.K. Martha, J. Nanda, G.M. Veith, N.J. Dudney, Surface studies of high voltage lithium rich composition: $Li_{1.2}Mn_{0.525}Ni_{0.175}Co_{0.1}O_2$, J. Power Sources 216 (2012) 179–186, https://doi.org/10.1016/j.jpowsour.2012.05.049.
[71] W. Wang, Y. Sun, P. Wen, Y. Zhou, D. Zhang, C. Chang, Mitigating the Jahn–Teller effect and enhancing the conductivity of O3-type $NaNi_{1/3}Fe_{1/3}Mn_{1/3}O_2$ cathode through Mn replacement with Sc for high-performance sodium-ion batteries, J. Alloys Compd. 994 (2024) 174585, https://doi.org/10.1016/j.jallcom.2024.174585.
[72] B. Xie, Y. Du, Y. Ma, S. Liu, Y. Wang, P. Zuo, Y. Gao, G. Yin, Interface reinforcement of a prussian blue cathode using a non-flammable Co-solvent cresyl diphenyl

phosphate for a high-safety Na-ion battery, ACS Sustain Chem Eng 9 (2021) 5809–5817, https://doi.org/10.1021/acssuschemeng.0c07853.
[73] Y. Gan, P. Ping, J. Wang, Y. Song, W. Gao, Comparative analysis of thermal stability and electrochemical performance of $NaNi_{1/3}Fe_{1/3}Mn_{1/3}O_2$ cathode in different electrolytes for sodium ion batteries, J. Power Sources 594 (2024) 234008, https://doi.org/10.1016/j.jpowsour.2023.234008.
[74] E. Sahadeo, J. Song, K. Gaskell, N. Kim, G. Rubloff, S.B. Lee, Investigation of the water-stimulated $Mg^{2+}$ insertion mechanism in an electrodeposited $MnO_2$ cathode using X-ray photoelectron spectroscopy, Phys. Chem. Chem. Phys. 20 (2018) 2517–2526, https://doi.org/10.1039/C7CP06312A.
[75] P. Bai, Y. He, X. Zou, X. Zhao, P. Xiong, Y. Xu, Elucidation of the sodium-storage mechanism in hard carbons, Adv. Energy Mater. 8 (2018) 1703217, https://doi.org/10.1002/aenm.201703217.
[76] J.-Y. Hwang, S.-T. Myung, D. Aurbach, Y.-K. Sun, Effect of nickel and iron on structural and electrochemical properties of O3 type layer cathode materials for sodium-ion batteries, J. Power Sources 324 (2016) 106–112, https://doi.org/10.1016/j.jpowsour.2016.05.064.
[77] H. Yoshida, N. Yabuuchi, S. Komaba, $NaFe_{0.5}Co_{0.5}O_2$ as high energy and power positive electrode for Na-ion batteries, Electrochem. Commun. 34 (2013) 60–63, https://doi.org/10.1016/j.elecom.2013.05.012.
[78] M. Jeong, H. Lee, J. Yoon, W.-S. Yoon, O3-type $NaNi_{1/3}Fe_{1/3}Mn_{1/3}O_2$ layered cathode for Na-ion batteries: Structural evolution and redox mechanism upon Na (de) intercalation, J. Power Sources 439 (2019) 227064, https://doi.org/10.1016/j.jpowsour.2019.227064.
[79] D. Di Lecce, D. Campanella, J. Hassoun, Insight on the enhanced reversibility of a multimetal layered oxide for sodium-ion battery, J. Phys. Chem. C 122 (2018) 23925–23933, https://doi.org/10.1021/acs.jpcc.8b07596.
[80] D.A. Stevens, J.R. Dahn, High capacity anode materials for rechargeable sodium-ion batteries, J. Electrochem. Soc. 147 (2000) 1271, https://doi.org/10.1149/1.1393348.
[81] X. Dou, I. Hasa, D. Saurel, C. Vaalma, L. Wu, D. Buchholz, D. Bresser, S. Komaba, S. Passerini, Hard carbons for sodium-ion batteries: structure, analysis, sustainability, and electrochemistry, Mater. Today 23 (2019) 87–104, https://doi.org/10.1016/j.mattod.2018.12.040.
[82] S. Passerini, D. Bresser, A. Moretti, A. Varzi, Batteries: Present and Future Energy Storage Challenges, Wiley-VCH Verlag, Weinheim, Germany, GmbH & Co. KGaA, 2020.
[83] T. Waldmann, C. Hogrefe, M. Flügel, I. Pivarníková, C. Weisenberger, E. Delz, M. Bolsinger, L. Boveleth, N. Paul, M. Kasper, M. Feinauer, R. Schäfer, K. Bischof, T. Danner, V. Knoblauch, P. Müller-Buschbaum, R. Gilles, A. Latz, M. Hölzle, M. Wohlfahrt-Mehrens, Efficient workflows for detecting Li depositions in lithium-ion batteries, J. Electrochem. Soc. 171 (2024) 070526, https://doi.org/10.1149/1945-7111/ad5ef8.
[84] T. Waldmann, B.-I. Hogg, M. Wohlfahrt-Mehrens, Li plating as unwanted side reaction in commercial Li-ion cells – a review, J. Power Sources 384 (2018) 107–124, https://doi.org/10.1016/j.jpowsour.2018.02.063.